Citation for published version:
Zhou, J, Zhao, X, Zang, J, Geng, J & Sun, S 2023, 'Wave power extraction by an oscillating water column array embedded in comb-type breakwaters: Performance analysis and hydrodynamic mechanism', *Physics of Fluids*, vol. 35, no. 7, 077110. https://doi.org/10.1063/5.0154829

DOI:
10.1063/5.0154829

Publication date:
2023

Document Version
Peer reviewed version

Link to publication

This article may be downloaded for personal use only. Any other use requires prior permission of the author and AIP Publishing. The following article appeared in
Jiachun Zhou, Xuanlie Zhao, Jun Zang, Jing Geng, Sulong Sun; Wave power extraction by an oscillating water column array embedded in comb-type breakwaters: Performance analysis and hydrodynamic mechanism.
Physics of Fluids 1 July 2023; 35 (7): 077110
and may be found at https://doi.org/10.1063/5.0154829

University of Bath

Alternative formats
If you require this document in an alternative format, please contact:
openaccess@bath.ac.uk

General rights
Copyright and moral rights for the publications made accessible in the public portal are retained by the authors and/or other copyright owners and it is a condition of accessing publications that users recognise and abide by the legal requirements associated with these rights.

Take down policy
If you believe that this document breaches copyright please contact us providing details, and we will remove access to the work immediately and investigate your claim.

Download date: 15. Sep. 2023

Wave power extraction by an oscillating water column array embedded in comb-type breakwaters: Performance analysis and hydrodynamic mechanism

Jiachun Zhou[1](周加春), Xuanlie Zhao[1, 2, 3, *](赵玄烈), Jun Zang[4](臧军), Jing Geng[1, 2, 3](耿敬), Sulong Sun[5](孙苏龙)

1 College of Shipbuilding Engineering, Harbin Engineering University, Harbin, 150001, China

2 Nanhai Institute of Harbin Engineering University, Sanya, 572000, China

3 State Key Laboratory of Hydro-Power Equipment, Harbin, 150040, China

4 Department of Architecture and Civil Engineering, University of Bath, Bath, BA2 7AY, UK

5 Shanghai Merchant Ship Design and Research Institute, Shanghai, 201203, China

* Email address for correspondence: xlzhao@hrbeu.edu.cn

Abstract

Cost-sharing, space-sharing, and multi-function can be achieved through integrating wave energy converters into coastal defense facilities. In this paper, we consider a periodical array of oscillating water columns (OWCs) embedded in the coast-based comb-type breakwater in presence of the step bottom. Based on the linear potential flow theory and matched eigenfunction expansion method, a semi-analytical model for solving the diffraction and radiation problems of the periodic OWC array is developed. The mathematical model is verified using Haskind relations and energy conservation law. Parametrical studies are carried out to illustrate the hydrodynamic characteristics of the OWC array embedded in the comb-type breakwater. This study also reveals the constructive and destructive interference effects between the breakwater and OWCs. It is found that the wave amplification caused by the projecting caisson produces a constructive effect on the wave power extraction. The enhancement of wave power extraction corresponds to the wave amplification caused by the projection caissons. However, the inherent strong wave reflection caused by the caisson array weakens the wave power extraction, particularly in the sensitive frequency range (i.e., $2 < kh_1 < 5.5$ in present investigations).

Keywords: Oscillating water column; wave resonance; oblique waves; wave power extraction; breakwater

1. Introduction

The exploitation and utilization of wave energy can alleviate carbon emissions from fossil energy and promote the development of marine economy. Cost-sharing, space-sharing, and multi-function can be achieved through integrating wave energy converters into coastal defense facilities (Falcão and Henriques, 2016; Portillo Juan et al., 2022; Vicinanza et al., 2019; Zhao et al., 2019). Benefits can also be gained by increasing the efficiency of wave energy devices and reducing the wave loads on breakwaters (Zhao et al., 2022).

Wave energy devices primarily incorporate three types: oscillating water column (OWC), oscillating buoy, and overtopping (Falcão, 2010). Among these, the OWC stands out for its simplicity in system composition and exceptional reliability. Under the action of incident waves, the water column experiences periodic oscillations, which drives the reciprocating flow in the air chamber and effectively extract wave power by implementing the air turbine. Evans (1978, 1982) pioneered the theoretical analysis on the hydrodynamics of OWC device. The wave power extraction performance of OWC embedded in caissons with projecting wall is examined by Malmo and Reitan (1985). Evans and Porter (1995) developed an efficient and accurate method to calculate the hydrodynamic coefficient of OWC in the 2-D case under context of linear water wave theory. Martins-Rivas and Mei (2009) theoretically investigate the influence of air compressibility on the performance of the OWC device. They point out that if the air chamber volume is large enough, the influence of air compressibility may dominate the wave power extraction performance and should not be ignored. Zheng et al. (2019) described a theoretical model for wave interaction with cylindrical OWC device situated on the coast. And parametrical investigations were conducted to examine the performance of the device. Rodríguez et al. (2021) illustrated the interaction between oblique waves and land-based OWCs based on potential flow theory. The radiation/diffraction problem is solved using the boundary element method. But, the length of the OWC caisson in along-shore direction is assumed to be infinite. Li et al. (2022) and Zhao et al. (2022) developed the semi-analytical model for wave interaction with OWC caisson array. Different to Rodríguez et al. (2021), the array effect is considered mathematically by introducing the periodical boundary conditions in Zhao et al. (2022). In addition, they found that the triggering of the along-shore sloshing resonance mitigates the hydrodynamic efficiency and significantly increases the wave loading on the wall.

Qin et al. (2013) experimentally investigated the pressure and wave amplification coefficient of OWC chamber with and without water channel. Results show that the existence of the water channel improves the wave power extraction performance of OWCs. Zhao et al. (2020, 2021) proposed the concept of integrating the oscillating buoy into the comb-type breakwater. Theoretical investigations demonstrate that the wave amplification effect led to the increment of the hydrodynamic efficiency of the wave energy device. In addition, the successful operation of Mutriku Wave Power Plant (Torre-Enciso et al., 2009) and REWEC3 breakwater (Arena et al., 2013) also confirm the feasibility of integrating OWC with breakwater.

It is known that topography significantly affect the wave propagation. The influence of topography on the hydrodynamic performance of OWC has also been widely concerned. Rezanejad et al. (2013) theoretically examined the influence of step bottom on the hydrodynamic performance of OWC situated on the step. It is found that the third resonance above the step broadens the efficient frequency bandwidth of the OWC. In further, Rezanejad et al. (2015) investigate the performance of the dual-chamber OWC on the step bottom. They point out that the presence of the step bottom may increase the hydrodynamic efficiency of the dual-chamber device. Ning et al. (2019) numerically investigated the hydrodynamic characteristics of a fixed OWC on the step bottom. John Ashlin et al. (2016) conducted experimental campaign to investigate the influence of different topographies in the chamber on the performance of the OWC device. Experimental data support that the topography does not affect the natural frequency of the OWC but modifies the efficiency. The above literature focus on the effect of the topography on performance of OWCs in 2-D scenarios.

In summary, extensive investigations have been conducted on the hydrodynamic characteristics of OWC devices and the influence of topography. However, the study of considering the effect of topography on array OWCs in 3-D scenarios has not been reported yet, and understanding the hydrodynamic characteristics in 3-D scenarios is crucial for practical engineering applications. Therefore, this paper aims to investigate the hydrodynamic characteristics of OWC arrays with step bottom conditions in 3-D case. And the corresponding mathematical model will be developed.

The paper is organized as follows. In Section 2, a detailed description of the mathematical model for the diffraction/radiation problem of waves interacting with OWCs

is provided, including the derivation of hydrodynamic efficiency and wave excitation volume flux. Section 3 verifies the mathematical model using Haskind relations and the conservation law of energy. Results are presented and discussed in Section 4. Finally, the key conclusions of the study are drawn in Section 5.

2. Mathematical model

2.1. Problem description

The schematic diagram of the investigated OWC-CTB (OWC-Comb type breakwater) is illustrated in Fig. 1. It consists of periodically arranged caissons projecting from the coast/cliff. Each pair of adjacent caissons creates a channel where an OWC chamber is situated. The OWC chamber utilizes the motion of the waves to generate air kinetic energy, which is then converted into useful energy by an air turbine.

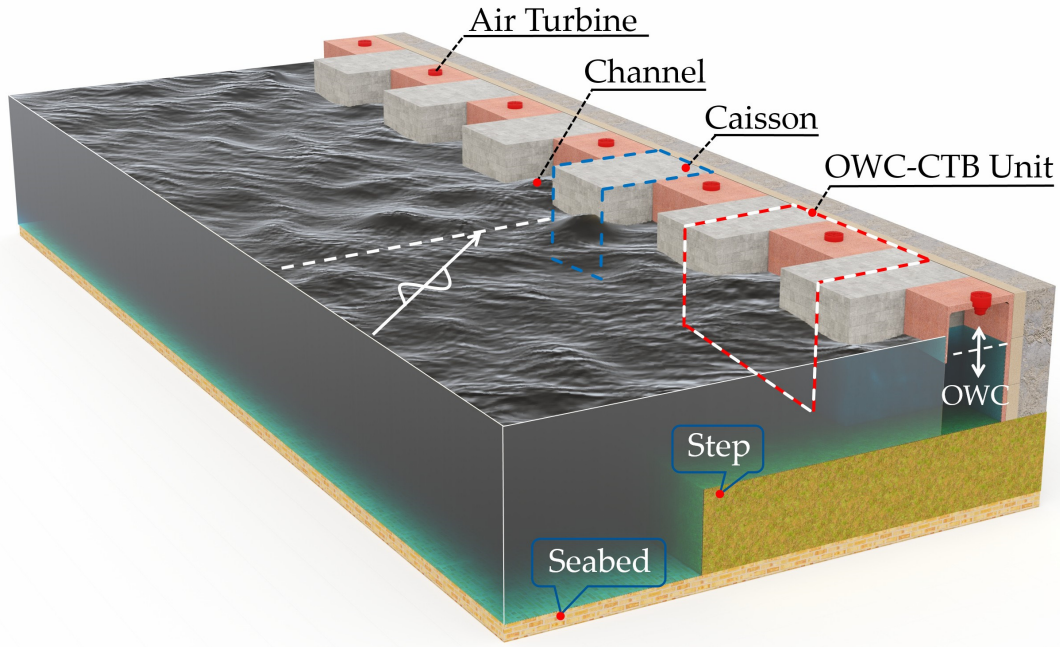

(a)

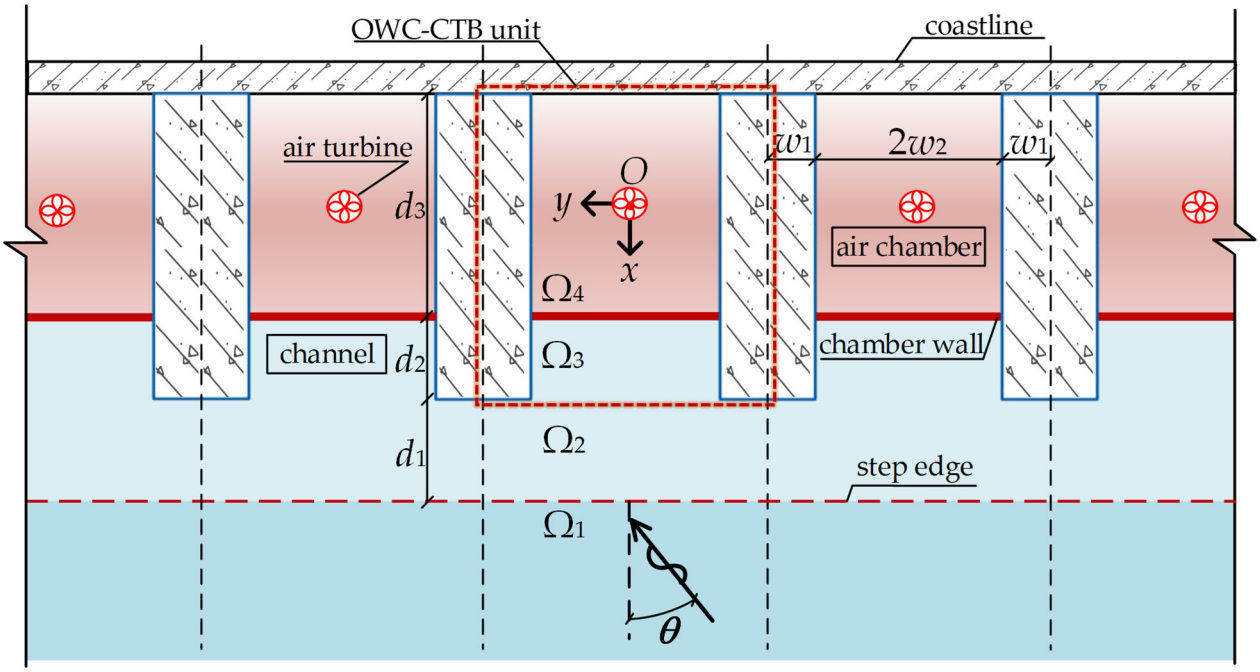

(b)

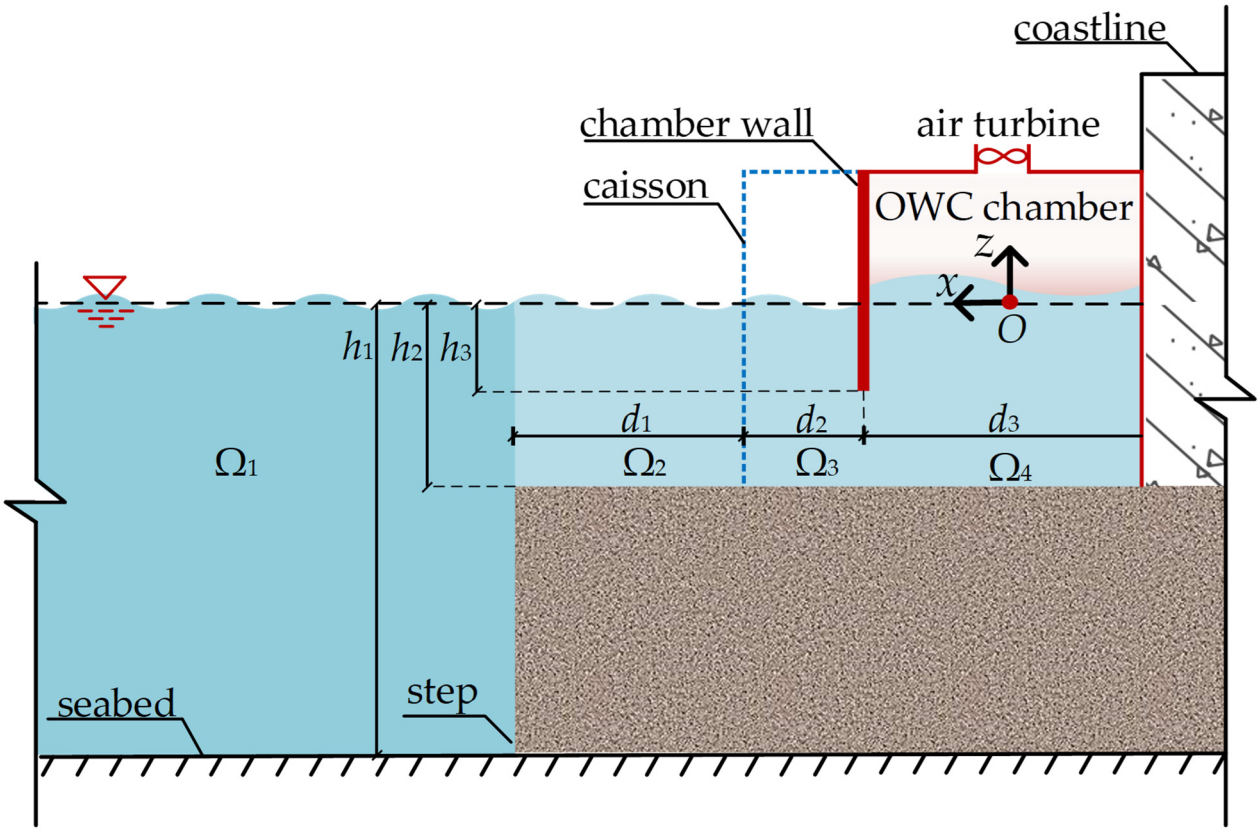

(c)

Fig. 1. Sketch of the OWC-CTB array (a) graphic description, (b) top view, (c) section view.

The mathematical model is developed based on the 3-D Cartesian coordinate system (*O*-*xyz*), where the origin *O* is located at the static water surface in the center of the OWC

chamber. As is shown in Fig. 1, the z- and y-axis are positive in the vertically upward direction and along straight coastline, respectively. The positive direction of O-x is perpendicular to the coastline. Symbolically, the variables of h_1, h_2, and h_3 correspond to water depth in region Ω_1, the water depth on the step, and the OWC wall draft, respectively. The parameters $2w_1$, $2w_2$, d_1, d_2, and d_3 represent the caisson width, the spacing between two adjacent caissons, the length of step, the distance between the chamber wall and caisson edge, and the length of the chamber, respectively. The fluid domain is divided into four subdomains, denoted as Ω_n (n = 1, 2, 3, 4). Specifically, Ω_1: $x_1 \le x$, $-B \le y \le B$, $-h_1 \le z \le 0$; Ω_2: $x_2 \le x \le x_1$, $-B \le y \le B$, $-h_2 \le z \le 0$; Ω_3: $x_3 \le x \le x_2$, $-w_2 \le y \le w_2$, $-h_2 \le z \le 0$; Ω_4: $x_4 \le x \le x_3$, $-w_2 \le y \le w_2$, $-h_2 \le z \le 0$, where the parameter $B = w_1 + w_2$.

2.2. Governing equations and boundary conditions

The fluid is assumed as incompressible, inviscid, and irrotational. The entire fluid field might be described by a time-dependent velocity potential $\varphi(x, y, z, t)$, and the time factor $e^{-i\omega t}$ can be factored out as,

$$\varphi(x,y,z,t) = \mathrm{Re}\left[\phi(x,y,z)\mathrm{e}^{-\mathrm{i}\omega t}\right], \tag{1}$$

where $\mathrm{i} = \sqrt{-1}$, ω denotes the angular frequency, ϕ denotes a complex space velocity potential independent of time t and satisfies the Laplace equation, i.e.,

$$\frac{\partial^2\phi}{\partial x^2} + \frac{\partial^2\phi}{\partial y^2} + \frac{\partial^2\phi}{\partial z^2} = 0. \tag{2}$$

The spatial velocity potential ϕ can be written as the superposition of an incident wave potential $\phi^{(I)}$, a diffracted wave potential $\phi^{(D)}$, and a radiated wave potential $\phi^{(R)}$, i.e.,

$$\phi_i = \phi^{(I)} + \phi^{(D)} + p\phi^{(R)}, \tag{3}$$

where the velocity potential of the incident wave is written as,

$$\phi^{(I)} = -\frac{\mathrm{i}gA}{\omega}\mathrm{e}^{-\mathrm{i}\left(k_x x - k_y y\right)}\frac{\cosh k\left(z+h_1\right)}{\cosh kh_1}. \tag{4}$$

The boundary conditions and periodical condition (Evans and Linton, 1993) for the scattering and radiated wave potentials can be written as,

$$\frac{\partial \phi_i^{(\ell)}}{\partial z}-\frac{\omega^2}{g}\phi_i^{(\ell)}=\begin{cases}0 & z=0;\ i=1,\ 2,\ 3\\ \dfrac{\mathrm{i}\omega\delta_{\ell,R}}{\rho g} & z=0;\ i=4\end{cases}, \tag{5}$$

$$\frac{\partial \phi_i^{(\ell)}}{\partial x}=0\ \begin{cases}i=1, & x=x_1,\ -B<y<B,\ -h_1<z<-h_2\\ i=2, & x=x_2,\ -B<y<-w_2\cup w_2<y<B,\ -h_2<z<0\\ i=3,4 & x=x_3,\ -w_2<y<w_2,\ -h_3<z<0\end{cases}, \tag{6}$$

$$\frac{\partial \phi_i^{(\ell)}}{\partial y}=0\ \begin{cases}i=3, & x_3<x<x_2,\ y=\pm w_2,\ -h_2<z<0\\ i=4, & x_4<x<x_3,\ y=\pm w_2,\ -h_2<z<0\end{cases}, \tag{7}$$

$$\frac{\partial \phi_i^{(\ell)}}{\partial z}=0\ \ z=-h_1,\ i=1 \text{ and } z=-h_2,\ i=2,\ 3,\ 4\ , \tag{8}$$

$$\phi_1^{(\ell)}\ \text{outgoing; finitevalue},\ \left|\sqrt{x^2+y^2}\right|\to\infty, \tag{9}$$

$$\phi_i^{(\ell)}\left[x,\ 2mB+y,\ z\right]=\mathrm{e}^{\mathrm{i}k_y 2mB}\phi_i^{(\ell)}\left(x,y,z\right), \tag{10}$$

where A, k, θ, and g are the incident wave amplitude, the incident wave number, the incident wave angle, and the gravitational acceleration, respectively. In this paper g = 9.81m/s^2, k_x = $k\cos\theta$, k_y = $k\sin\theta$. ℓ is denoted by the symbol of S or R, representing diffraction and radiation problem. $\delta_{\ell,R}$ is the Kronecker delta,

$$\delta_{\ell,R}=\begin{cases}1, & \ell=R\\ 0, & \ell\neq R\end{cases}. \tag{11}$$

2.3. Solutions to wave diffraction and radiation problem

According to the governing equation and boundary conditions, the expression of velocity potential in each subdomain is obtained by the method of separation of variables, i.e.,

$$\phi_1^{(\ell)}=-\frac{\mathrm{i}gA}{\omega}\left[\mathrm{e}^{-\mathrm{i}(x-x_1)k_x}\mathrm{e}^{\mathrm{i}yk_y}Z_1^{(1)}\left(z\right)+\sum_{m=-M}^{M}Y_m^{(1)}\left(y\right)\sum_{n=1}^{N}A_{mn}^{(\ell)}\mathrm{e}^{\lambda_{mn}^{(1)}(x-x_1)}Z_n^{(1)}\left(z\right)\right], \tag{12}$$

$$\phi_2^{(\ell)}=-\frac{\mathrm{i}gA}{\omega}\left[\sum_{m=-M}^{M}Y_m^{(1)}\left(y\right)\sum_{n=1}^{N}\left(B_{mn}^{(\ell)}\mathrm{e}^{\lambda_{mn}^{(2)}(x-x_1)}+C_{mn}^{(\ell)}\mathrm{e}^{-\lambda_{mn}^{(2)}(x-x_2)}\right)Z_n^{(2)}\left(z\right)\right], \tag{13}$$

$$\phi_3^{(\ell)}=-\frac{\mathrm{i}gA}{\omega}\left[\sum_{m=1}^{M}Y_m^{(2)}\left(y\right)\sum_{n=1}^{N}\left(D_{mn}^{(\ell)}\mathrm{e}^{\lambda_{mn}^{(3)}(x-x_2)}+E_{mn}^{(\ell)}\mathrm{e}^{-\lambda_{mn}^{(3)}(x-x_3)}\right)Z_n^{(2)}\left(z\right)\right], \tag{14}$$

$$\phi_4^{(\ell)} = -\frac{\mathrm{i}gA}{\omega}\left[\sum_{m=1}^{M} Y_m^{(2)}(y)\sum_{n=1}^{N}\left(F_{mn}^{(\ell)}\mathrm{e}^{\lambda_{mn}^{(3)}(x-x_3)} + G_{mn}^{(\ell)}\mathrm{e}^{-\lambda_{mn}^{(3)}(x-x_4)}\right)Z_n^{(2)}(z)\right] - \frac{\mathrm{i}\delta_{\ell,R}}{\rho\omega}, \tag{15}$$

where $A_{mn}^{(l)}$, $B_{mn}^{(l)}$, $C_{mn}^{(l)}$, $D_{mn}^{(l)}$, $E_{mn}^{(l)}$, $F_{mn}^{(l)}$, $G_{mn}^{(l)}$ are the unknown coefficient. The y-directional eigenfunctions are defined as,

$$Y_m^{(1)}(y) = \mathrm{e}^{\mathrm{i}\left(k_y + \pi m/B\right)y},\ m = 0,\ \pm 1,\ \pm 2,\ ...,\ \pm M, \tag{16}$$

$$Y_m^{(2)}(y) = \cos\left[\frac{(m-1)\pi}{2w_2}(w_2 - y)\right],\ m = 1,\ 2,\ ...,\ M, \tag{17}$$

the z-directional eigenfunctions are defined as,

$$Z_n^{(1)}(z) = \cos\left[k_n^{(1)}(z + h_1)\right] / \cos\left(k_n^{(1)}h_1\right),\ n = 1,\ 2,\ ...,\ N, \tag{18}$$

$$Z_n^{(2)}(z) = \cos\left[k_n^{(2)}(z + h_2)\right] / \cos\left(k_n^{(2)}h_2\right),\ n = 1,\ 2,\ ...,\ N, \tag{19}$$

and the x-directional eigenfunctions are defined as,

$$\lambda_{mn}^{(i)} = \begin{cases} -\sqrt{P_{m1}^{(i)}}, & P_{m1}^{(i)} \ge 0,\ m = 0, \pm 1, \pm 2, ..., \pm M;\ n = 1 \\ \mathrm{i}\sqrt{-P_{m1}^{(i)}}, & P_{m1}^{(i)} < 0,\ m = 0, \pm 1, \pm 2, ..., \pm M;\ n = 1 \\ -\sqrt{P_{mn}^{(i)}}, & P_{mn}^{(i)} \ge 0,\ m = 0, \pm 1, \pm 2, ..., \pm M;\ n = 2,\ 3, ..., N \end{cases}, \quad P_{mn}^{(i)} = \left(k_y + \pi m/B\right)^2 + \left(k_n^{(i)}\right)^2,\ i = 1,\ 2, \tag{20}$$

$$\lambda_{mn}^{(3)} = \begin{cases} \sqrt{P_{m1}^{(3)}}, & P_{m1}^{(3)} \ge 0,\ m = 1,\ 2, ..., M;\ n = 1 \\ \mathrm{i}\sqrt{-P_{m1}^{(3)}}, & P_{m1}^{(3)} < 0,\ m = 1,\ 2, ..., M;\ n = 1 \\ \sqrt{P_{mn}^{(3)}}, & P_{mn}^{(3)} \ge 0,\ m = 1,\ 2, ..., M;\ n = 2,\ 3, ..., N \end{cases}, \quad P_{mn}^{(3)} = \left[(m-1)\pi/2w_2\right]^2 + \left(k_n^{(2)}\right)^2. \tag{21}$$

The eigenvalues of $k_1^{(i)}$ and $k_n^{(i)}$ ($n \ge 2$) satisfied the dispersion relation of $\omega^2 = g\kappa_1^{(i)}\tanh\kappa_1^{(i)}h_i$ and $\omega^2 = -gk_n^{(i)}\tan k_n^{(i)}h_i$ ($n \ge 2$), respectively; $\kappa_1^{(1)} = k$, $k_1^{(i)} = -\mathrm{i}\kappa_1^{(i)}$, $i = 1, 2$.

In order to deal with the square root singularity of fluid velocity at the tip of the thin chamber wall, the fluid velocity at $x = x_3$ is expressed as (Evans and Porter, 1995),

$$U_{x=x_3} = -\frac{\mathrm{i}gA}{\omega}\left[\sum_{m=1}^{M} Y_m^{(2)}(y)\sum_{q=1}^{Q} Q_{mq}^{(\ell)} u_{x=x_3,q}(z)\right], \tag{22}$$

where $Q_{mq}^{(\ell)}$ is the unknown coefficient. $u_{x=x3,q}(z)$ is determined by the following formula,

$$u_{x=x_3,q}(z) = \frac{2(-1)^{q-1}}{\pi\sqrt{(h_2 - h_3)^2 - (z + h_2)^2}}\, T_{2(q-1)}\left(\frac{z + h_2}{z - h_3}\right), \tag{23}$$

where $T_{2(q-1)}[(z+h_2)/(z-h_3)]$ is the even term of Chebyshev polynomials.

Here, the matched eigenfunction expansion method is applied to solve both the wave diffraction and radiation problems. According to the velocity and pressure continuity in adjacent subdomains, the equations for solving unknown coefficients can be established. The velocity continuity satisfies Eqs. (24)~(28), and the pressure continuity satisfies Eqs. (29)~(31). For simplicity, the corresponding details of the solution based on the continuity conditions are given in Appendix A.

$$\frac{\partial \phi_1^{(\ell)}}{\partial x}=\begin{cases}0, & \left(x=x_1,\ -B<y<B,\ -h_1<z<-h_2\right)\\ \dfrac{\partial \phi_2^{(\ell)}}{\partial x}, & \left(x=x_1,\ -B<y<B,\ -h_2<z<0\right)\end{cases}, \tag{24}$$

$$\frac{\partial \phi_2^{(\ell)}}{\partial x}=\begin{cases}0, & \left(x=x_2,\ -B<y<-w_2\cup w_2<y<B,\ -h_2<z<0\right)\\ \dfrac{\partial \phi_3^{(\ell)}}{\partial x}, & \left(x=x_2,\ -w_2<y<w_2,\ -h_2<z<0\right)\end{cases}, \tag{25}$$

$$\frac{\partial \phi_3^{(\ell)}}{\partial x}=\begin{cases}0, & \left(x=x_3,\ -w_2<y<w_2,\ -h_3<z<0\right)\\ U_{x=x_3}, & \left(x=x_3,\ -w_2<y<w_2,\ -h_2<z<-h_3\right)\end{cases}, \tag{26}$$

$$\frac{\partial \phi_4^{(\ell)}}{\partial x}=\begin{cases}0, & \left(x=x_3,\ -w_2<y<w_2,\ -h_3<z<0\right)\\ U_{x=x_3}, & \left(x=x_3,\ -w_2<y<w_2,\ -h_2<z<-h_3\right)\end{cases}, \tag{27}$$

$$\frac{\partial \phi_4^{(\ell)}}{\partial x}=0,\ \left(x=x_4,\ -w_2<y<w_2,\ -h_2<z<0\right), \tag{28}$$

$$\phi_1^{(\ell)}=\phi_2^{(\ell)},\ \left(x=x_1,\ -B<y<B,\ -h_2<z<0\right), \tag{29}$$

$$\phi_2^{(\ell)}=\phi_3^{(\ell)},\ \left(x=x_2,\ -w_2<y<w_2,\ -h_2<z<0\right), \tag{30}$$

$$\phi_3^{(\ell)}=\phi_4^{(\ell)},\ \left(x=x_3,\ -w_2<y<w_2,\ -h_2<z<-h_3\right). \tag{31}$$

2.4. Hydrodynamic parameters

2.4.1. Volume flux inside pneumatic chamber

The excitation volume flux Q_S can be obtained by the integral of the vertical water velocity along the free surface inside the chamber. Accordingly, the radiation volume flux Q_R under forced motion can also be obtained similarly. The specific calculations are shown as

$$Q_i = \int_{-w_2}^{w_2}\int_{x_3}^{x_4} \frac{\partial\left(\phi_4^{(\ell)}\right)}{\partial z}\mathrm{d}x\mathrm{d}y = \frac{2\mathrm{i}gAw_2}{\omega}\sum_{n=1}^{N}\frac{\left(1-\mathrm{e}^{-2\lambda_{1,n}^{(3)}x_3}\right)\left(F_{1,n}^{(\ell)}+G_{1,n}^{(\ell)}\right)k_n^{(2)}\tan k_n^{(2)}h_2}{\lambda_{1,n}^{(3)}},\ i=\mathrm{S},\mathrm{R}\ . \tag{32}$$

The radiation conductance c and the radiation susceptance μ are defined as c = -Re (Q_{R}) and μ = Im (Q_{R}), respectively. According to the Haskind relations (Falnes and Kurniawan, 2020), the excitation volume flux can also be calculated from the far-field radiated waves, i.e.,

$$Q_{\mathrm{r}} = \frac{2\rho g\omega A^2 B}{k}\left[1+\frac{2kh_1}{\sinh\left(2kh_1\right)}\right]\cos\theta\left|A_{M+1,1}^{(R)}\right|. \tag{33}$$

2.4.2. Hydrodynamic efficiency and reflection coefficient

The air pressure inside the chamber can be calculated as,

$$p = \frac{Q_{\mathrm{S}}}{c+c_{\mathrm{PTO}}-\mathrm{i}\left(\mu+\mu_{\mathrm{PTO}}\right)}, \tag{34}$$

where c_{PTO} represents the PTO damping implemented on the chamber, μ_{PTO} corresponds to the effects of air compressibility, and the air compression process is isentropic. The optimal PTO damping is written as,

$$c_{\mathrm{PTO}} = \sqrt{c^2+\left(\mu+\mu_{\mathrm{PTO}}\right)^2}\ , \tag{35}$$

where $\mu_{\mathrm{PTO}} = \omega V / c_a^2\rho_0$, c_a (= 340m/s) denotes the sound velocity in the air, ρ_0 (= 1kg/m^3) is the static air density, and initial air volume inside the pneumatic chamber is given by V = $0.2w_2d_3h_2$.

The time-averaged wave power extraction over one wave period can be expressed as,

$$P_{\max} = \frac{1}{2}c_{\mathrm{PTO}}p^2\ . \tag{36}$$

The incident waves power can be written as,

$$P_{\mathrm{incident}} = \frac{\rho g\omega A^2 B}{2k}\left(1+\frac{2kh}{\sinh 2kh}\right). \tag{37}$$

The hydrodynamic efficiency corresponding to chamber can be calculated as,

$$\eta = \frac{P_{\max}}{P_{\mathrm{incident}}}\ . \tag{38}$$

The wave reflection coefficient can be obtained by

$$C_{\mathrm{r}}=\left[\sum_{m=-M_1}^{m=M_2}\left(A_{m1}^{(S)}+pA_{m1}^{(R)}\right)^2\left(1-\left(\sin\theta+m\pi/kB\right)^2\right)^{1/2}/\cos\theta\right]^{1/2}, \tag{39}$$

where $M_1=\mathrm{int}[(1+\sin\theta)kB/\pi]$ and $M_2=\mathrm{int}[(1-\sin\theta)kB/\pi]$, the int[ ] denotes the floor function.

3. Model verification

In this section, the Haskind relation and energy conservation law is used to verify the mathematical model. The geometrical parameters are fixed as $h_1=10$ m, $h_2/h_1=0.4$, $h_3/h_1=0.1$, $d_1/h_1=1$, $d_2/h_1=0.5$, $d_3/h_1=0.3$, $w_1/h_1=0.2$, $w_2/h_1=0.3$. The optimal PTO damping (see Eq.(35)) is used to calculate the extracted power, and unless otherwise stated, the optimal damping will also be employed throughout this paper. Truncations of $N=5$, $M=20$, and $Q=5$ were made to guarantee the convergence of the model. The Haskind relation is employed to verify the semi-analytical solution of the diffraction and radiation problem (Falnes and Kurniawan, 2020). Fig. 2(a) present the comparisons of the excitation volume flux $\bar{Q}_{\mathrm{S}}$ and $\bar{Q}_{\mathrm{r}}$, calculate as Eqs. (32) and (33). The quantities of Q_{S} and Q_{R} is normalized as $\bar{Q}_i=|Q_i|/2\omega A w_2 d_3$, $i=\mathrm{S},\mathrm{R}$. It is observed that the two aspects exhibit good agreement, which may verify the solution of the diffraction/radiation problem. Furthermore, we present the results of η, C_{r}, and $C_{\mathrm{r}}^2+\eta$ in Fig. 2(b). The satisfaction of $C_{\mathrm{r}}^2+\eta=1$ confirms the derivation of the reflection coefficient and hydrodynamic efficiency.

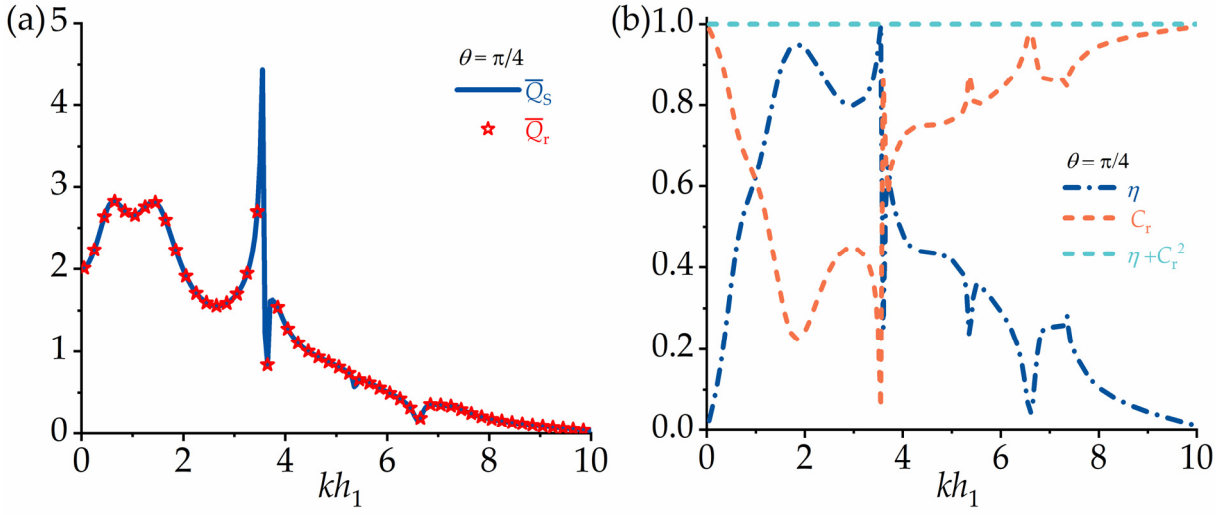

Fig. 2. Results of (a) $\bar{Q}_{\mathrm{S}}$, $\bar{Q}_{\mathrm{r}}$; (b) η, C_{r}, and $C_{\mathrm{r}}^2+\eta$ versus wave number kh_1 for $\theta=\pi/4$.

4. Results and discussions

After validation, comprehensive parametric investigations will be conducted in this section to reveal the impact of key parameters on the performance of the present wave energy system.

4.1. Effect of the step bottom

Fig. 3 demonstrates the results of hydrodynamic efficiency η, reflection coefficient C_r, dimensionless excitation volume flux $\bar{Q}_S$, dimensionless radiation conductance $\bar{c}$, and dimensionless radiation susceptance $\bar{\mu}$ for different step sizes (h_2/h_1 = 0.2, 0.4, 0.6, 0.8, 1.0). The other geometrical and physical parameters are as follows: $h_3 = 0.1h_1$, $d_1 = h_1$, $d_2 = 0.5h_1$, $d_3 = 0.3h_1$, $w_1 = 0.2h_1$, $w_2 = 0.3h_1$, and $\theta = 0$. The normalization method for needed dimensionless physical quantities is given by $\left[\bar{c},\ \bar{\mu},\ \bar{\mu}_{\mathrm{PTO}}\right] = \dfrac{\rho g}{2\omega w_2 d_3}\left[c,\ \mu,\ \mu_{\mathrm{PTO}}\right]$.

From Fig. 3(a-b), it is observed that the influence of steps on the hydrodynamic performance of the system becomes more pronounced when the step depth is relatively small (h_2/h_1<0.4). However, when the step depth is large, its impact is not significant. Generally, the curve of η exhibits two peaks at $kh_1 \approx 2.6$ and $kh_1 \approx 4.53$. Correspondingly, two valley values are found for the reflection coefficient. Specifically, for the case of $h_2/h_1 = 0.2$, the trend of η and C_r demonstrate strong oscillations throughout the whole frequency range. That is to say, when the step depth is small, strong hydrodynamic interactions occur between the step, the caisson, and the OWC.

To further evaluate the characteristics of the water column embedded in the breakwaters, we plot the $\bar{Q}_S$ in Fig. 3(c). Similar to the trend of η and C_r, it can be found that, as h_2/h_1 decreases, stronger oscillations can be found for the curve. It is worth noting that $\bar{Q}_S$ for h_2/h_1 = 0.2 is obviously greater than that corresponds to the other cases at the lower frequency region, which can explain the strong oscillations of η and C_r in the low frequency region (kh_1 < 2).

The multiple peaks of η in presence of the step bottom is also reported by Rezanejad et al. (2013) for the two-dimensional case. Our results in Fig. 3 confirm that there exist multiple peaks in 3-Dcase, which may be attributed to the third resonance (i.e., wave resonance above the step) above the step. It is noted that the peak value appears at $kh_1 \approx 0.5$ (i.e., $\omega \approx 0.48$).

Based on Newton's second law and hydrostatic theory, assuming the water column behaves as a rigid body, the natural frequency ω_3 corresponding to the third resonance on the step can be expressed as

$$\omega_3 = \sqrt{\frac{g w_2 h_2}{d_2 w_2 d_3 + d_1 (w_1 + w_2) d_3}}. \tag{40}$$

For the current study, the natural frequency of the third resonance is approximately $\omega \approx 0.48$ for $h_2/h_1 = 0.2$, which differs from the value obtained from Eq.(40), $\omega_3 \approx 0.55$. This discrepancy arises due to the fact that the confined water in subdomain Ω_2 cannot be strictly considered as a rigid body. Additionally, the radiation conductance represents the ability of extracting wave power by OWC (Rezanejad et al., 2013). As depicted in Fig. 3(d, e), the wave power extraction performance of the OWC weakens as h_2/h_1 become smaller.

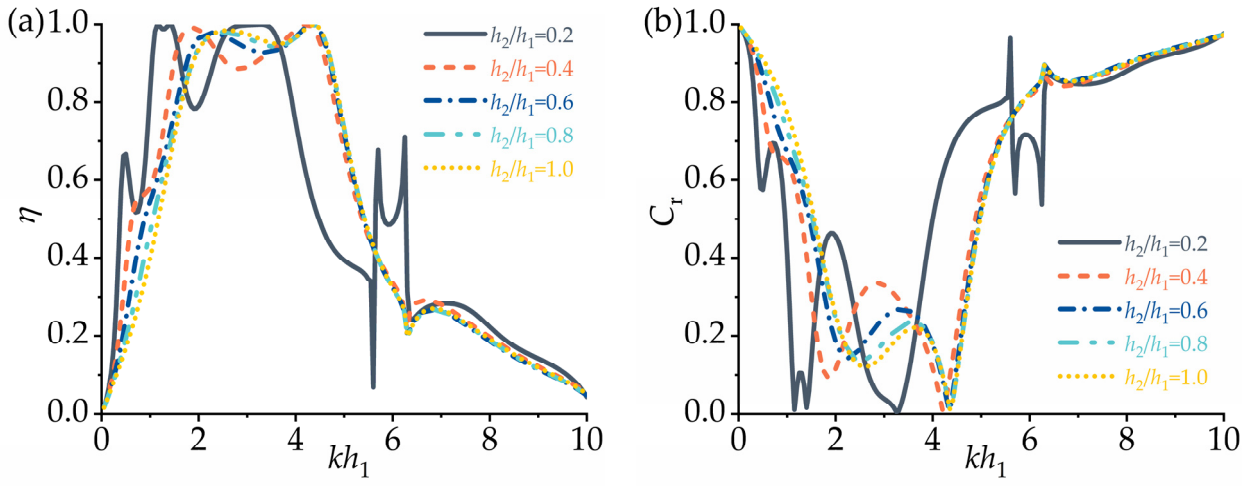

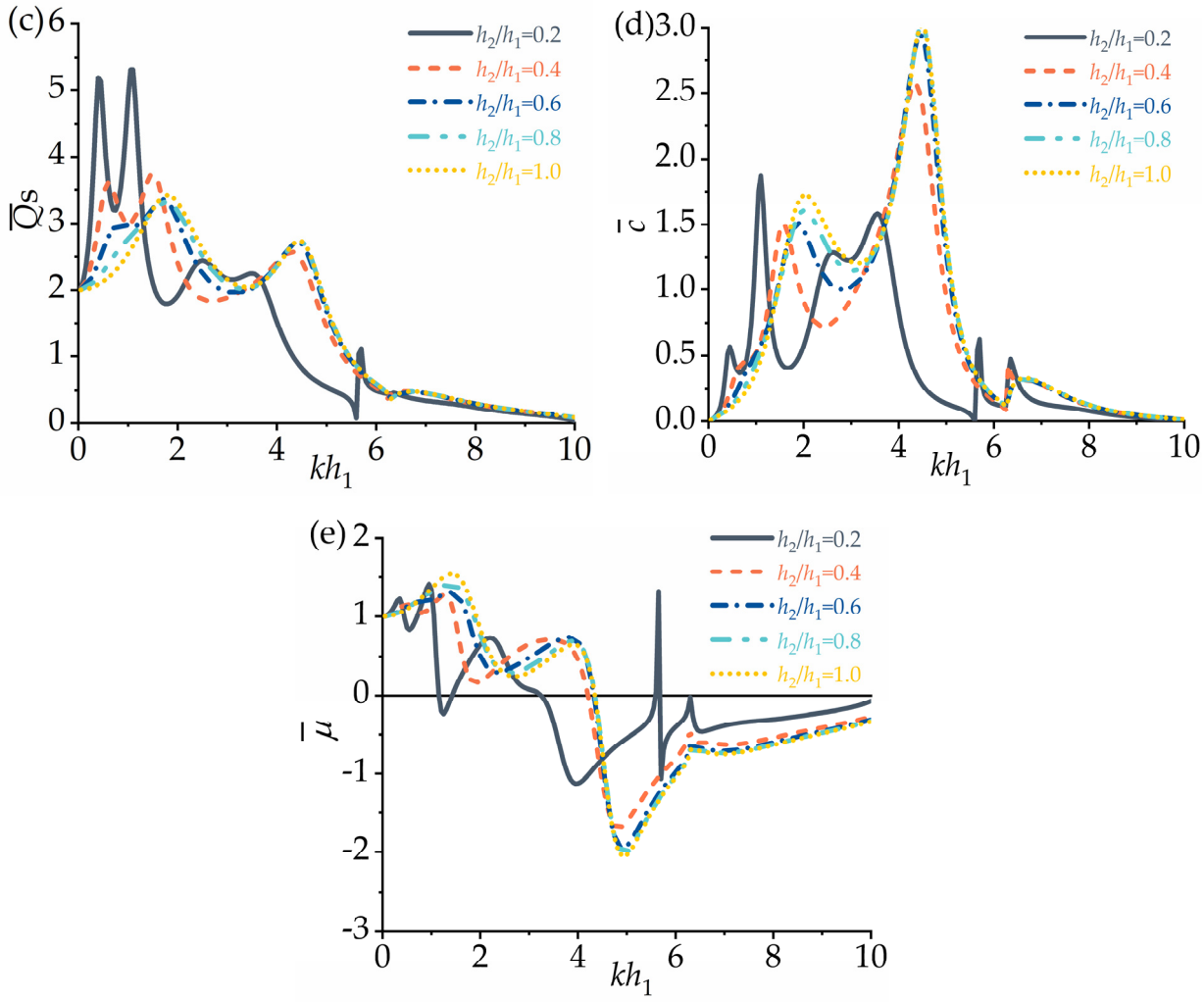

Fig. 3. (a) Hydrodynamic efficiency η, (b) reflection coefficient C_r, (c) dimensionless excitation volume flux $\bar{Q}_S$, (d) dimensionless radiation conductance $\bar{c}$, and (e) dimensionless radiation susceptance $\bar{\mu}$ versus dimensionless wave number kh_1 for h_2/h_1 = 0.2, 0.4, 0.6, 0.8, and 1.0.

4.2. Effect of the incident wave angle

In order to illustrate the performance of OWC-CTB system under oblique waves, we plot the results of hydrodynamic efficiency η, dimensionless excitation volume flux $\bar{Q}_S$, dimensionless radiation conductance $\bar{c}$, and radiation susceptance $\bar{\mu}$ for different incident wave angles (θ = 0, π/12, π/6, π/4, π/3, 5π/12) in Fig. 4. The other geometrical and physical parameters are as follows: $h_2 = 0.4h_1$, $h_3 = 0.1h_1$, $d_1 = h_1$, $d_2 = 0.5h_1$, $d_3 = 0.3h_1$, $w_1 = 0.2h_1$, and $w_2 = 0.3h_1$.

As is shown in Fig. 4(a), it is found that the incident wave angle significantly affects the hydrodynamic efficiency of OWC-CTB at the relatively higher frequency region (i.e., 2 < kh_1 < 5.5 here), which is referred to as the sensitive frequency range in this study. The second

peak of η decreases with increasing θ, leading to a narrower effective frequency bandwidth (i.e., frequency range corresponding to $\eta > 50\%$). But, θ slightly modifies the first peak of η, which is attributed to wave amplification in the water channel (i.e., region Ω_3 in Fig. 1(b)). That is to say, the influence of wave amplification on the performance of the embedded OWCs is slightly affected by the incident wave angle.

Furthermore, in the low-frequency region, the oscillating volume flux is more sensitive to the incident wave angle (as shown in Fig. 4(c)). However, the influence of θ on the overall variation trend of radiation conductance and radiation susceptance is weak (as depicted in Fig. 4(d, e)). But the location of the peaks changes as θ varies.

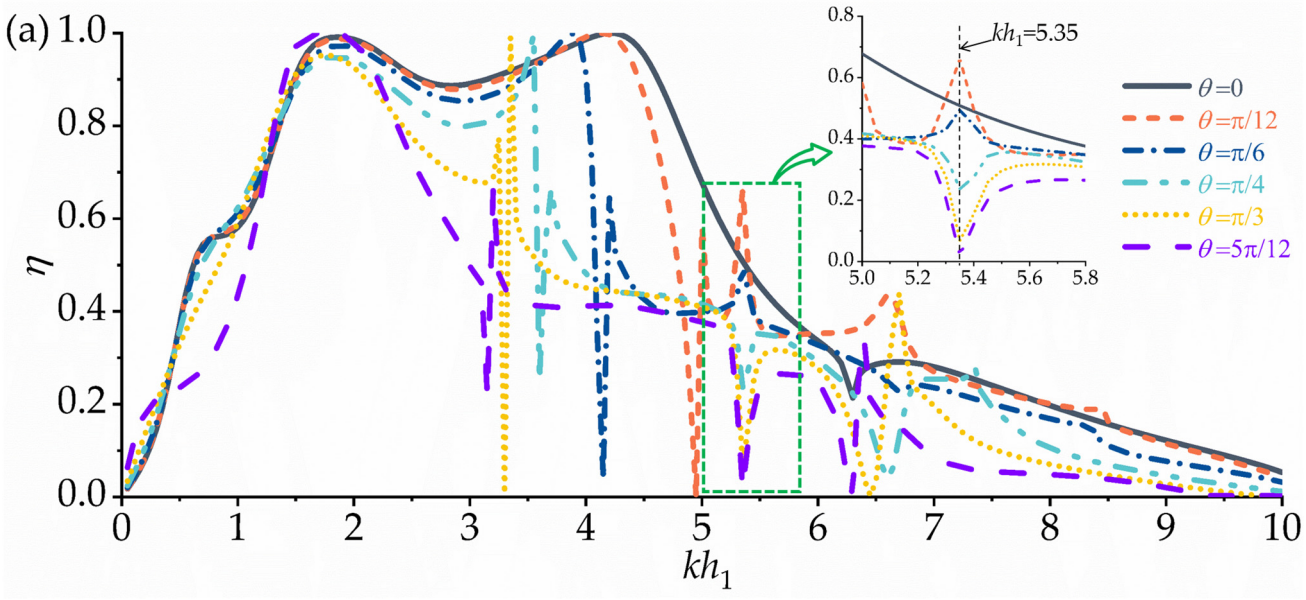

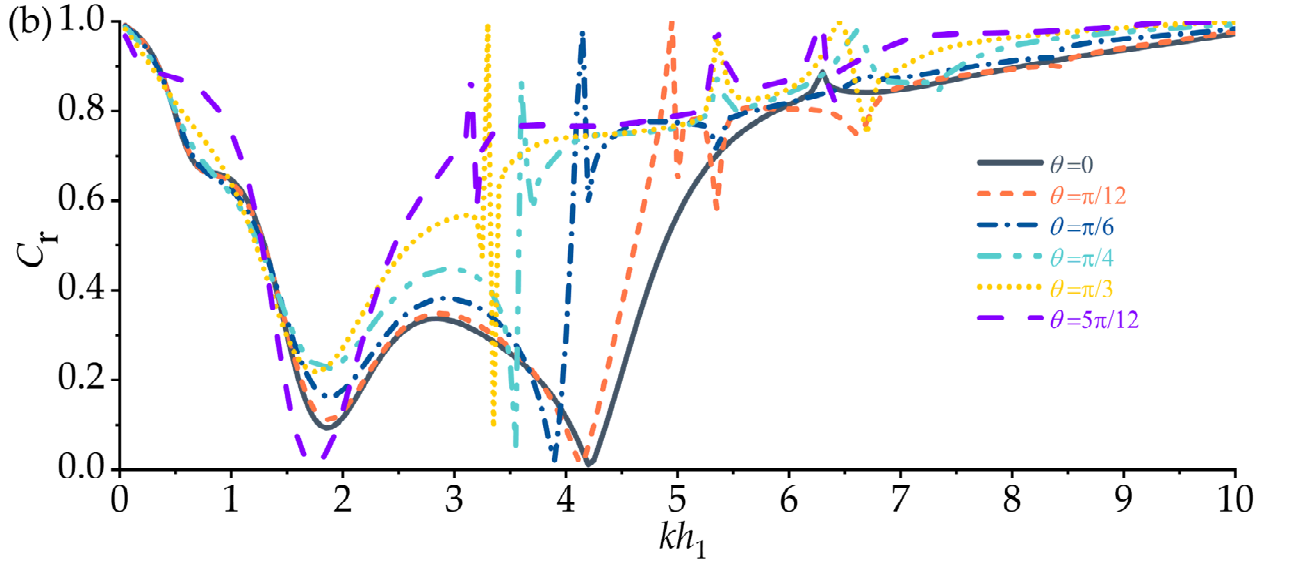

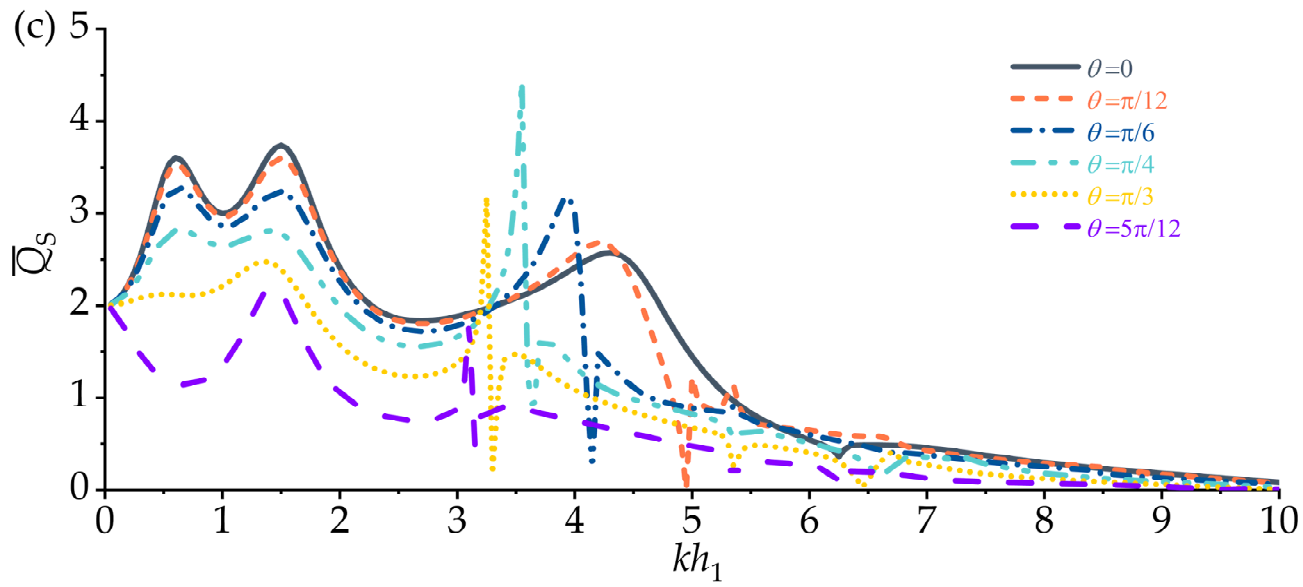
(c)
$\overline{Q}_S$
kh_1
θ=0
θ=π/12
θ=π/6
θ=π/4
θ=π/3
θ=5π/12

300

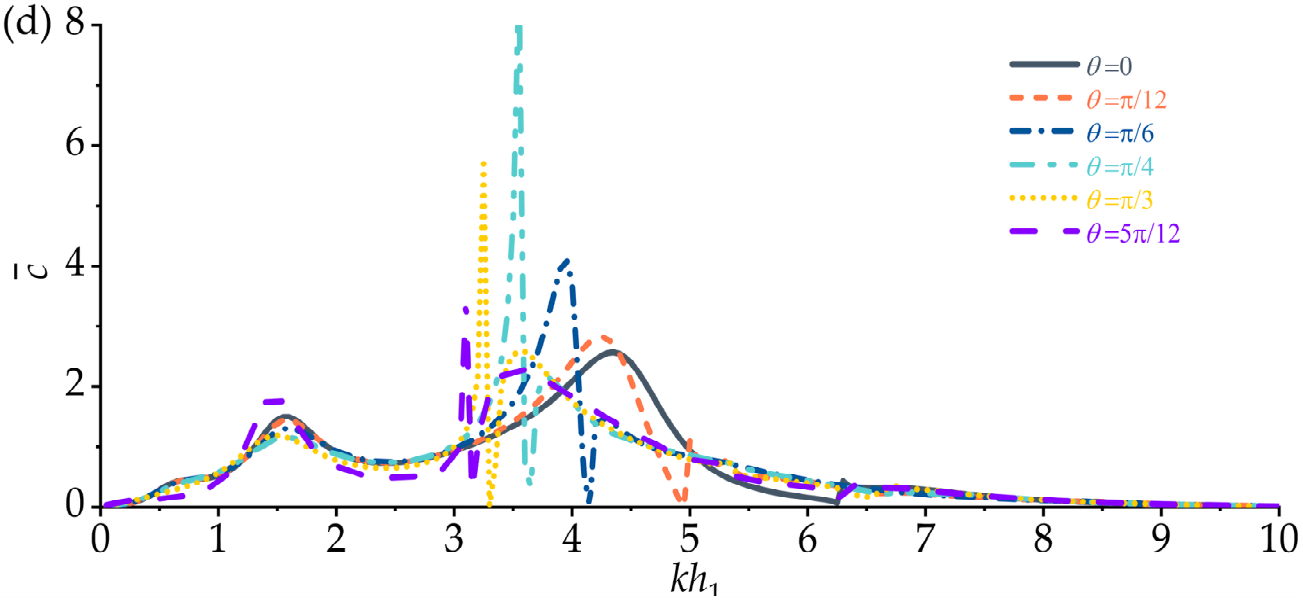
(d)
$\overline{c}$
kh_1
θ=0
θ=π/12
θ=π/6
θ=π/4
θ=π/3
θ=5π/12

301

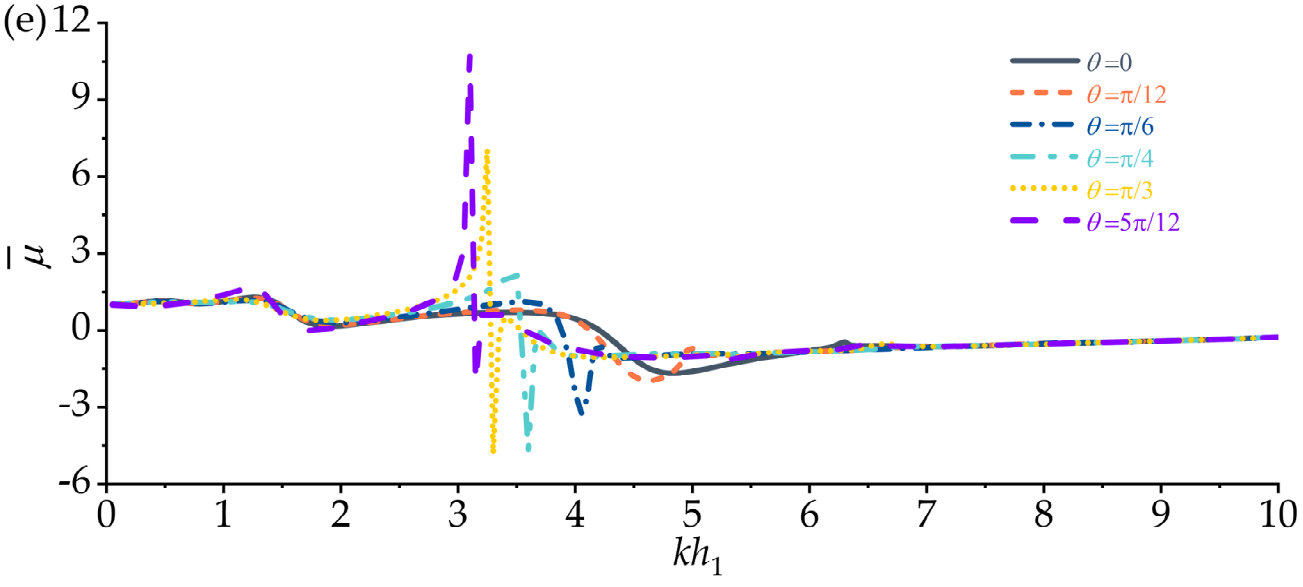
(e)
$\overline{\mu}$
kh_1
θ=0
θ=π/12
θ=π/6
θ=π/4
θ=π/3
θ=5π/12

302

Fig. 4. (a) Hydrodynamic efficiency η, (b) reflection coefficient C_r, (c) dimensionless excitation volume flux $\bar{Q}s$, (d) dimensionless radiation conductance $\bar{c}$, and (e) dimensionless radiation susceptance $\bar{\mu}$ versus dimensionless wave number kh_1 for $\theta = 0$, $\pi/12$, $\pi/6$, $\pi/4$, $\pi/3$, and $5\pi/12$.

Interestingly, the hydrodynamic efficiency curve changes abruptly at $kh_1 \approx 6.28$ ($\theta = 0$)、4.99 ($\theta = \pi/12$)、4.19 ($\theta = \pi/6$)、3.68 ($\theta = \pi/4$)、3.37 ($\theta = \pi/3$)、and 3.20 ($\theta = 5\pi/12$), which corresponds to the condition of $kB = |m\pi/(1\pm\sin\theta)|$, $m = 1$ (Rayleigh, 1907). Notably, this king of wave resonance results in strong wave reflection and reduced power extraction (see Fig. 4(a, b)). Fig. 5 shows the wave amplitude distribution for case of kh_1=3.68 and $\theta = \pi/4$. Due to periodic arrangement of OWC-CTB in the y-direction, the wave amplitude of one OWC-CTB unit can be extended to any other units multiplying the phase difference of $e^{2ik_y mB}$. The surface wave amplitude in different fluid subdomains (Ω_n, $n = 1, 2, 3, 4$) are given by,

$$\zeta_n = \left| \frac{i\omega}{g} \left(\phi_n^{(S)} + p\phi_n^{(R)} \right) \right|, \quad n = 1,\ 2,\ 3,\ 4\,. \tag{41}$$

It is instinctively found that, when condition of $kB = |\pi/(1\pm\sin\theta)|$ are meet, the wave height inside the OWC chamber is not significantly amplified. And we observe strong wave reflection phenomena at the weather side. The wave amplitude decays visually, the wave amplitude decays as distance from the OWC array increases.

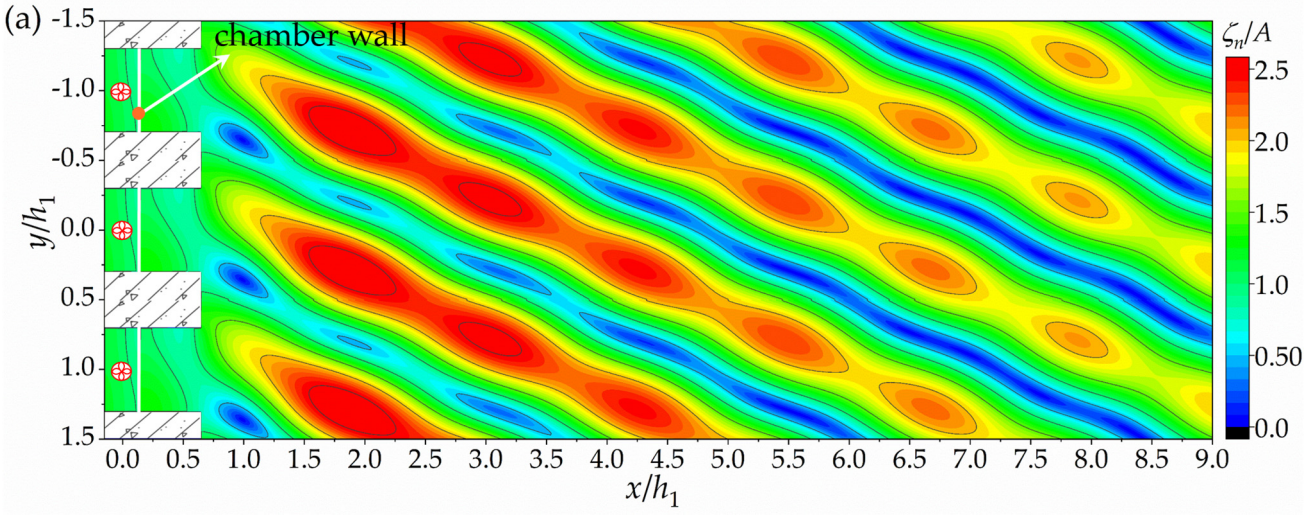

Fig. 5. The wave amplitude distribution in the multi-order modes at the oblique wave, (a) first-order mode for $kh_1 = 3.68$, $\theta = \pi/4$.

Fig. 6 presents the number of propagating modal waves in different fluid subdomains (Ω_n, $n = 1, 2, 3, 4$) under $\theta = \pi/4$ condition. Within the range of $3.48 < kh_1 < 3.68$, the number of propagating modal waves in subdomain Ω_2 is greater than that in subdomains Ω_1 and Ω_3,

indicating the occurrence of trapped wave phenomenon in subdomain Ω_2, leading to abrupt changes in hydrodynamic coefficients and key physical quantities, such as η and C_r. The total number of the propagating modal waves in different fluid subdomains (Ω_n, n = 1, 2, 3, 4) can be calculated as

$$M_{\text{total}} = \begin{cases} \text{int}\left[\left(k + k_y\right)B/\pi\right] + \text{int}\left[\left(k - k_y\right)B/\pi\right] + 1 & \text{in } \Omega_1 \\ \text{int}\left[\left(\text{i}k_1^{(2)} + k_y\right)B/\pi\right] + \text{int}\left[\left(\text{i}k_1^{(2)} - k_y\right)B/\pi\right] + 1 & \text{in } \Omega_2 \\ \text{int}\left[2\text{i}w_2 k_1^{(2)}/\pi\right] + 1 & \text{in } \Omega_3 \text{ and } \Omega_4 \end{cases}. \tag{42}$$

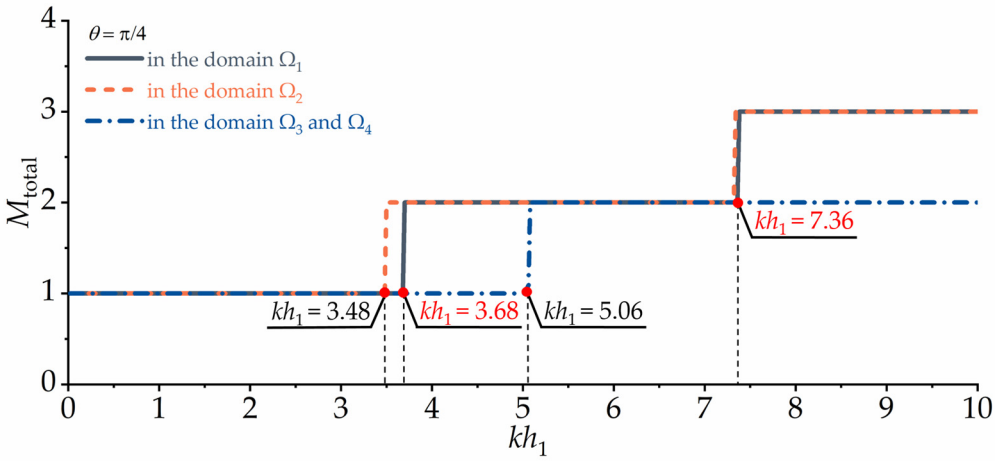

Fig.6 Number of propagating modal waves at different fluid subdomains for $\theta = \pi/4$

Furthermore, it is noteworthy that the hydrodynamic efficiency exhibits different trends at $kh_1 \approx 5.35$ for various incident wave angle considered here. From Fig. 7(a), the water column exhibit a near piston-mode motion in case of $\theta = 0$, and the hydrodynamic efficiency curve shows no abrupt changes. However, for $\theta = \pi/12$, the water inside the chamber undergoes a partially asymmetric oscillatory motion (refer to Fig. 7(b)), resulting in a sudden increase in hydrodynamic efficiency, which is not observed in OWC array without the projecting caisson (Li et al., 2022). Fig. 7(c) demonstrates that at $\theta = 5\pi/12$, the oscillatory motion in the y-direction inside the chamber becomes nearly symmetric, and the hydrodynamic efficiency approaches 0.

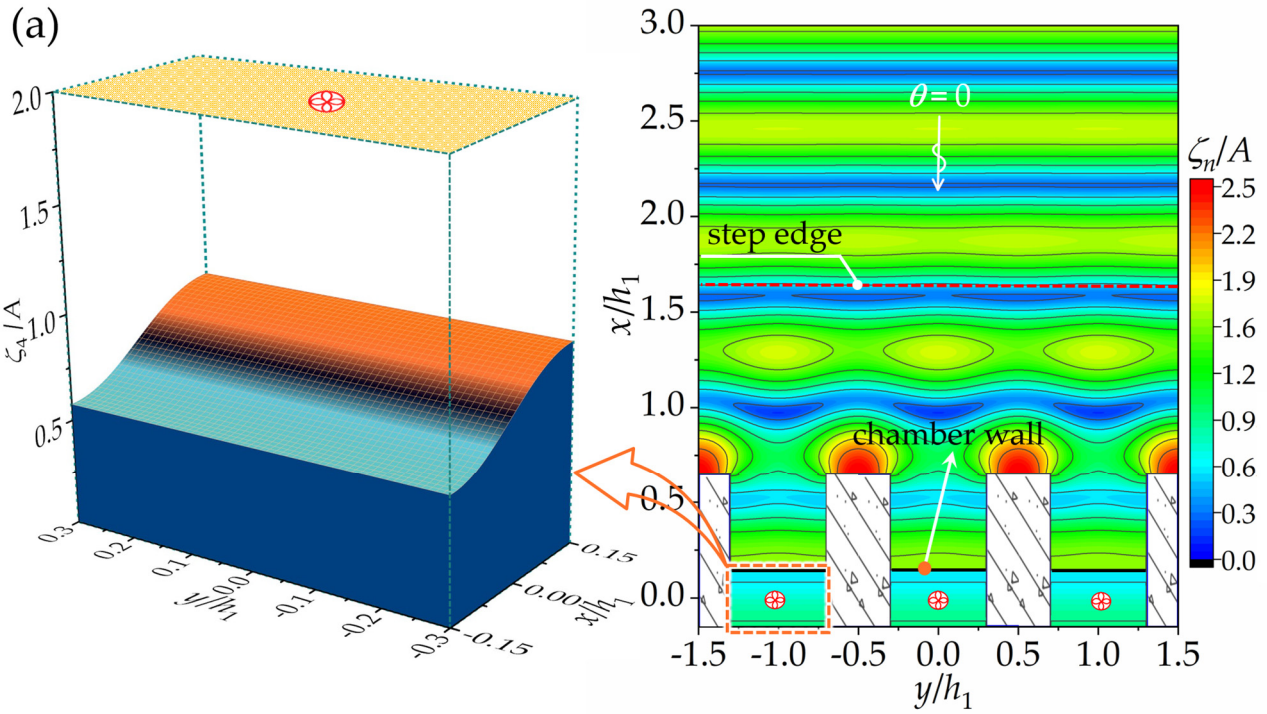
(a)
θ = 0
step edge
chamber wall
ζn/A
x/h1
y/h1

341

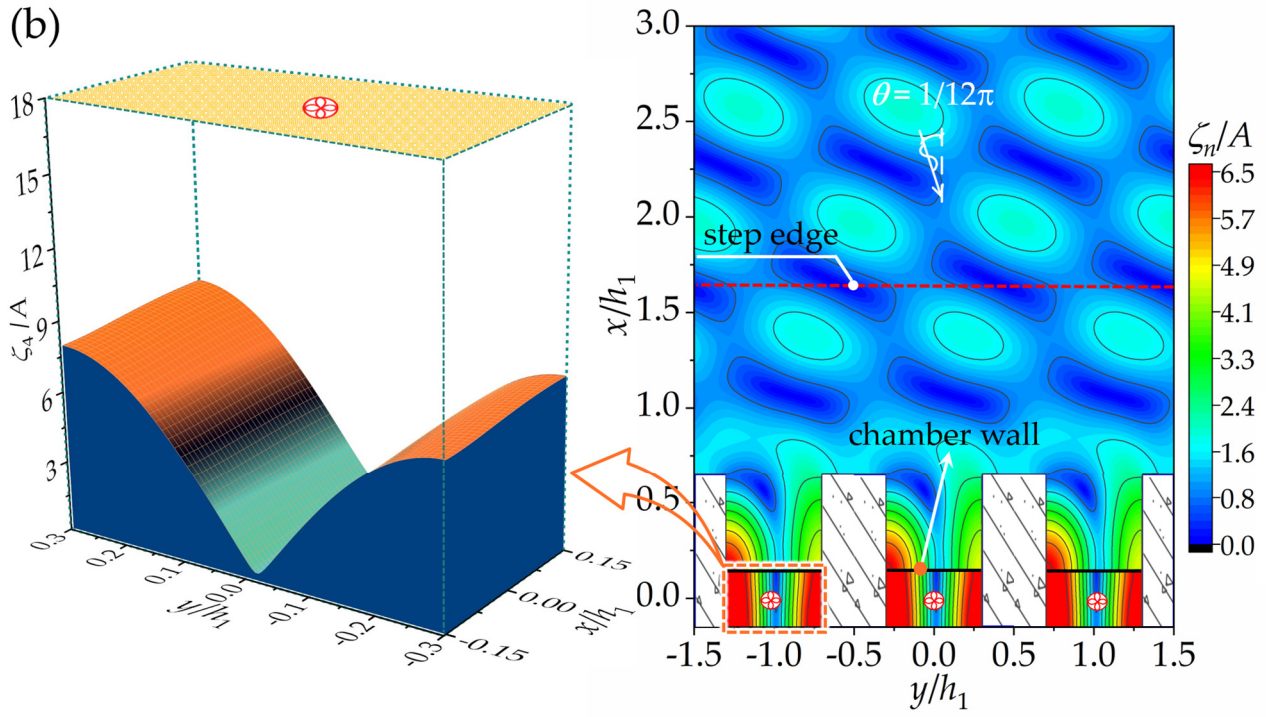
(b)
θ = 1/12π
step edge
chamber wall
ζn/A
x/h1
y/h1

342

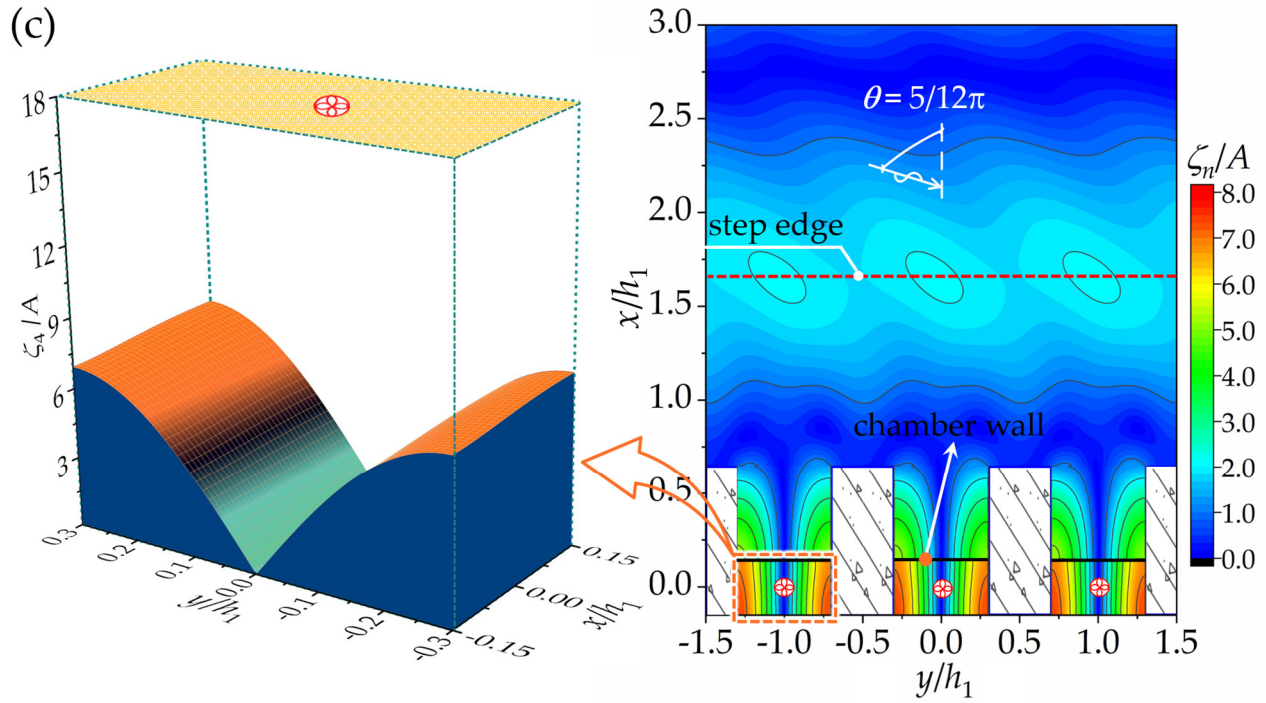

Fig. 7. Wave amplitude distributions for case of (a) $\theta = 0$, $kh_1 = 5.35$, (b) $\theta = \pi/12$, $kh_1 = 5.35$, (c) $\theta = 5\pi/12$, $kh_1 = 5.35$.

4.3. Discussion on wave amplification induced by channel and its influence on power extraction

In order to reveal the channel effect on the OWC system, we plot the results of hydrodynamic efficiency η and dimensionless radiation volume flux $\bar{Q}_S$ for $d_2/d_3 = 0$, 5/6, 5/3, 5/2, and 10/3. The other geometrical and physical parameters are as follows: $h_2 = 0.4h_1$, $h_3 = 0.1h_1$, $d_1 = h_1$, $d_3 = 0.3h_1$, $w_1 = 0.2h_1$, and $w_2 = 0.3h_1$.

As shown in Fig. 8(a), multiple peaks of efficiency were observed as the d_2/d_3 increases. Specifically, d_2/d_3 = 5/2, the hydrodynamic efficiency peaked at $kh_1 \approx 1.5$, 3.45, and 5.7, respectively. The influence of d_2/d_3 on hydrodynamic efficiency is mainly reflected in the frequency range of ($kh_1 < 6.3$). It is noted that $kh_1 = 6.3$ corresponds to the condition of $kB = |\pi/(1\pm\sin\theta)|$. For the range of $kh_1 > 6.3$, the hydrodynamic efficiency was significantly mitigated due to the presence of strong wave reflection. Nevertheless, the effective frequency bandwidth ($\eta > 0.5$) was broadened as $d_2/d_3 > 0$. Within the present calculations, the optimal ratio belongs to $d_2/d_3 = 5/2$. Notably, the effective bandwidth comprises as the d_2/d_3 continues to increase. For $\bar{Q}_S$, in the range of $k < 6.3$, it exhibits strong oscillation phenomena with

relatively constant amplitudes. The oscillation positions correspond exactly to the peak positions of the efficiency.

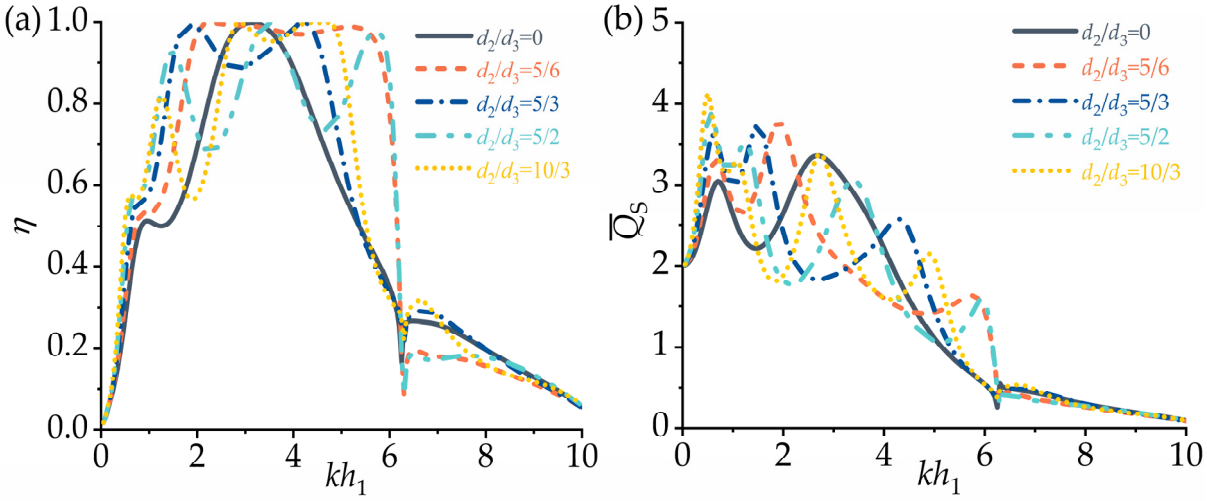

Fig. 8. (a) Optimal hydrodynamic efficiency η and (b) dimensionless excitation volume flux $\bar{Q}_S$ versus dimensionless wave number kh_1 for d_2/d_3 = 0, 5/6, 5/3, 5/2, 10/3.

In order to illustrate the mechanism behind the multi-peak phenomenon in efficiency, Fig. 9 present results of $-\bar{\mu}_{PTO}$, $\bar{\mu}$, η, $\bar{c}$ and $\bar{c}_{d2/d3} - \bar{c}_k$ for d_2/d_3 = 5/6, 5/3, 5/2, and 10/3. Please note that $\bar{c}_k$ represent the value of $\bar{c}$ for d_2/d_3 = 0. From Fig. 9, it can be observed that the peaks of hydrodynamic efficiency align with that of $\bar{c}$ and $\bar{c}_{d2/d3}$-$\bar{c}_k$. Specifically, for d_2/d_3 = 5/2 (see Fig. 9(c)), the hydrodynamic efficiency exhibits peaks at $kh_1 \approx 1.5$, 3.45, and 5.7, coinciding with the peaks of $\bar{c}$ and $\bar{c}_{d2/d3}$-$\bar{c}_k$. That means that radiating wave energy capability of the OWC reaches its peaks at those locations, leading to the peaks in hydrodynamic efficiency. Besides, it should be noted that the curve of $-\bar{\mu}_{PTO}$ versus kh_1 and $\bar{\mu}$ versus kh_1 intersect at $kh_1 \approx 3.45$. Similar phenomena have also been found in Martins-Rivas and Mei (2009). However, in Martins-Rivas and Mei (2009), they observed the dual-peak efficiency phenomenon caused by the significant air compressibility inside the chamber, specifically when the condition $-\bar{\mu}_{PTO} = \bar{\mu}$ is satisfied. This differs from the multi-peak efficiency phenomenon observed in Fig. 9. Since the chamber volume considered here is relatively small (i.e., $V = 0.2w_2d_3h_2$), the influence of air compressibility is attenuated. In this paper, the condition $-\bar{\mu}_{PTO} = \bar{\mu}$ contributes only one peak, while the remaining peaks are attributed to the wave amplification induced by the projecting caissons (refer to Fig. 10). Similar phenomena are observed for other cases of d_2/d_3, indicating that this multi-peak phenomenon is caused by the projecting caissons.

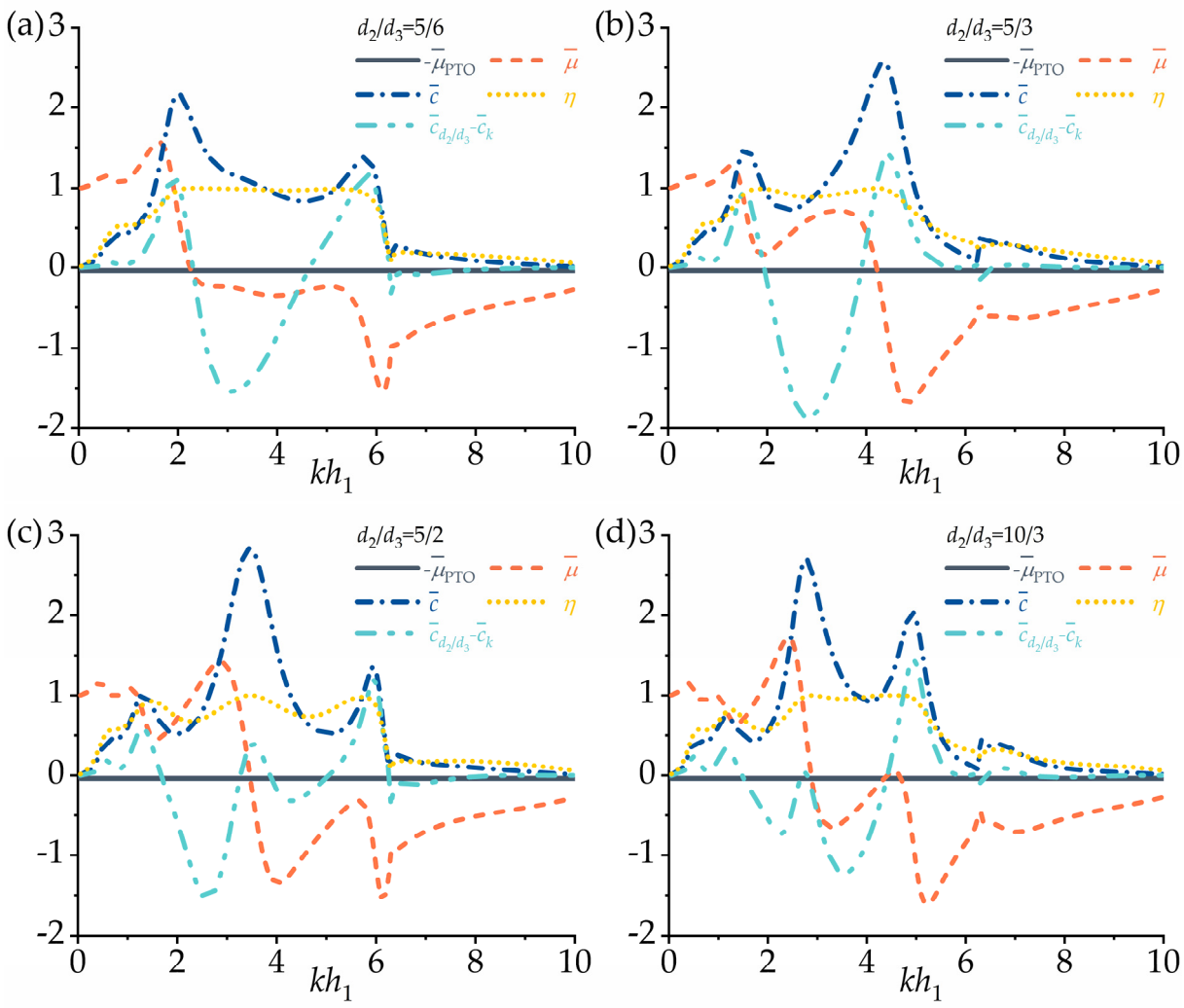

Fig. 9. Results of dimensionless air compression damping $-\bar{\mu}_{PTO}$, dimensionless radiation susceptance $\bar{\mu}$, Optimal hydrodynamic efficiency η, dimensionless radiation conductance $\bar{c}$, and $\bar{c}_{d2/d3}$-$\bar{c}_k$ versus dimensionless wave number kh_1 for (a) d_2/d_3 = 5/6, (b) d_2/d_3 = 5/3, (c) d_2/d_3 = 5/2, and (d) d_2/d_3 = 10/3.

The hydrodynamic performance of OWC-CTB is affected by the wave motion in the channel (i.e., Ω_3 in Fig. 1(b)). Fig. 10 shows results of the amplitude amplification factor in the channel and hydrodynamic efficiency for d_2/d_3 = 5/2. The amplification factor of wave amplitude in the channel can be calculated according to the following formula(Wang et al., 2017)

$$R=\left|\cos k_1^{(2)}d_2-\frac{k_1^{(2)}w_2}{4}\left(\mathrm{i}-\frac{2}{\pi}\ln\frac{\gamma k_1^{(2)}w_2}{\sqrt{2}\mathrm{e}^{3/2}}\right)\sin k_1^{(2)}d_2\right|^{-1}, \tag{43}$$

where γ = 1.781 is the index of the Euler constant.

Fig. 10 presents the results of R and η. It can be observed that the wave height in the water channel reaches its maximum at $kh_1 \approx 1.5$ and 5.7, corresponding to the first and second modes (Wang et al., 2011). These two modes coincide with the locations of the peaks in efficiency, which is the physical reason for the occurrence of the two peaks in efficiency. Therefore, it can be concluded that the multi-peak phenomenon in efficiency of the CTB-OWC system is caused by the amplified wave motion inside the channel.

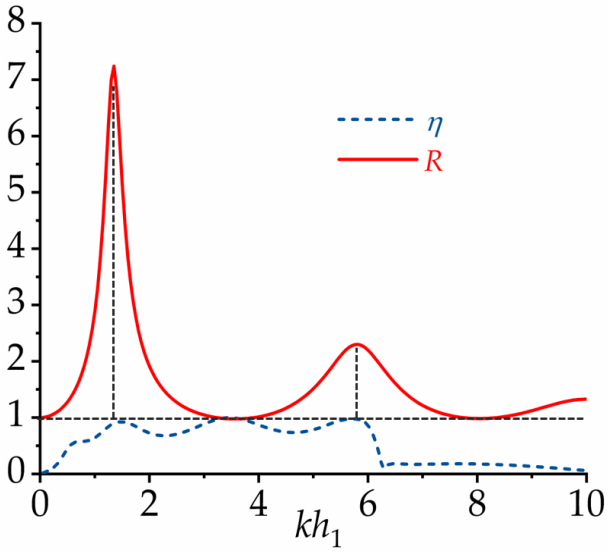

Fig. 10 Amplitude amplification factor R in the channel and hydrodynamic efficiency η curve at $d_2/d_3 = 5/2$.

5. Conclusions

The hydrodynamic performance of OWC-CTB unit array on step bottom was modeled analytically based on the linear wave theory and the method of matched eigenfunction expansion. The velocity singularity at the tip of the thin chamber wall was resolved by introducing the Galerkin technique. The assumed linear optimum PTO model was implemented to obtain the wave power and efficiency. The semi-analytical solution of the diffraction and radiation problems is verified using Haskind relation, and the derivation of reflection coefficient and hydrodynamic efficiency is verified based on the energy conservation law. Since the model is developed based on linear potential theory, the wave nonlinearity and fluid viscous effect are not considered, which may lead to the overestimate of the power extraction. But the resonant characteristics of the OWC and the influence of the dominant factor were predicted reasonably using potential-flow based tool. The

418 experimental campaign or high-resolution numerical investigation is needed to evaluate the
419 nonlinear aspects.
420 In the three-dimensional mathematical model, the resonance of the water column on the
421 step is triggered with the increase of the step height. The incident wave angle is the key
422 controlling factor for the wave absorption performance of the OWC-CTB. It is found that the
423 change of incident wave angle triggers a variety of wave resonances at a specific frequency.
424 Interestingly, the increase/inhibition of hydrodynamic efficiency by sloshing resonance in the
425 y-direction of the air chamber is closely related to the incident wave angle. The amplitude
426 amplification in the channel improves wave energy extraction efficiency, which triggers the
427 peak value of hydrodynamic efficiency in the chamber and broadens the efficient frequency
428 bandwidth of OWC-CTB. The following conclusions can be drawn from this study:
429 1) Based on the linear potential flow theory and matched eigenfunction expansion
430 method, a three-dimensional mathematical model was proposed to describe the
431 wave scattering and radiation inside and outside OWC-CTB array under oblique
432 waves. The semi-analytical solutions are validated by the wave energy conservation
433 law and the Haskind relations.
434 2) With the increase of the step bottom height, the hydrodynamic efficiency and wave
435 reflection coefficient show multiple oscillations. It should be noted that the curve
436 oscillation in the low frequency region is due to the wave resonance on the step.
437 Oscillations at other frequencies may be due to the fact that the hydrodynamic
438 interactions between the step bottom and the OWC-CTB significantly modify the
439 hydrodynamic characteristics of the water column.
440 3) The action of oblique waves triggers multi-order modes for wave resonance and
441 leads to strong wave reflection. The increase of incident wave angle reduces the
442 energy component of the wave in the x-direction, and the piston resonance intensity
443 in the chamber gradually decreases, while the efficient frequency bandwidth also
444 narrows. Interestingly, due to the incomplete symmetry of the chamber structure,
445 with the increases of incident wave angle, the sloshing resonance first increases and
446 then decreases the hydrodynamic efficiency of OWC-CTB. The interaction between
447 the incident wave at any angle and the chamber after refraction through the channel
448 will not affect the trigger frequency of the sloshing resonance in the y-direction.

4) The channel formed between adjacent caissons can gather waves and amplify the wave amplitude, and this wave amplification triggers peaks in hydrodynamic efficiency and significantly broadens the efficient bandwidth. It is found that this hydrodynamic peak occurs because the longitudinal oscillation modes in the channel increase the radiation conductance of the OWC-CTB and thus improve the ability to extract wave energy. In addition, research shows that the triggering frequency of peak hydrodynamic efficiency may be related to the longitudinal oscillation mode in the channel.

Acknowledgments

The work is supported by the following project grants, National Natural Science Foundation of China (52001086; 52271270), Key Research and Development Program of Hainan (ZDYF2023GXJS017).

Appendix A: Integral equations

By substituting Eqs. (12) and (13) into Eq.(24), multiplying both sides by $\overline{Y}_u^{(1)}(y)\cdot Z_v^{(1)}(z)$ and integrating over the range $y\in[-B, B]$, $z\in[-h_1, 0]$, we obtain

$$\begin{aligned}&\int_{-h_1}^{0}\int_{-B}^{B}\left[-\mathrm{i}k_x\mathrm{e}^{-\mathrm{i}(x-x_1)k_x}\mathrm{e}^{\mathrm{i}yk_y}Z_1^{(1)}(z)+\sum_{m=-M}^{M}Y_m^{(1)}(y)\sum_{n=1}^{N}A_{mn}^{(\ell)}\lambda_{mn}^{(1)}\mathrm{e}^{\lambda_{mn}^{(1)}(x-x_1)}Z_n^{(1)}(z)\right]\overline{Y}_u^{(1)}(y)Z_v^{(1)}(z)\mathrm{d}y\mathrm{d}z\\&=\int_{-h_2}^{0}\int_{-B}^{B}\left[\sum_{m=-M}^{M}Y_m^{(2)}(y)\sum_{n=1}^{N}\left(B_{mn}^{(\ell)}\lambda_{mn}^{(2)}\mathrm{e}^{\lambda_{mn}^{(2)}(x-x_1)}-\lambda_{mn}^{(2)}C_{mn}^{(\ell)}\mathrm{e}^{-\lambda_{mn}^{(2)}(x-x_2)}\right)Z_n^{(2)}(z)\right]\overline{Y}_u^{(1)}(y)Z_v^{(1)}(z)\mathrm{d}y\mathrm{d}z\end{aligned},\tag{A.1}$$

where $\overline{Y}_u^{(1)}(y)$ represents the conjugate function of $Y_u^{(1)}(y)$. By separating the unknown coefficient matrix, we have:

$$X_{mn}^{(1)}+A_{mn}^{(\ell)}Q_{mn}^{(1)}=B_{mn}^{(\ell)}Q_{mn}^{(2)}+C_{mn}^{(\ell)}Q_{mn}^{(3)},\tag{A.2}$$

where

$$Q_{mn}^{(1)}=\int_{-h_1}^{0}\int_{-B}^{B}\left[\sum_{m=-M}^{M}Y_m^{(1)}(y)\sum_{n=1}^{N}A_{mn}^{(\ell)}\lambda_{mn}^{(1)}\mathrm{e}^{\lambda_{mn}^{(1)}(x-x_1)}Z_n^{(1)}(z)\right]\overline{Y}_u^{(1)}(y)Z_v^{(1)}(z)\mathrm{d}y\mathrm{d}z,\tag{A.3}$$

$$Q_{mn}^{(2)}=\int_{-h_2}^{0}\int_{-B}^{B}\left[\sum_{m=-M}^{M}Y_m^{(2)}(y)\sum_{n=1}^{N}\lambda_{mn}^{(2)}\mathrm{e}^{\lambda_{mn}^{(2)}(x-x_1)}Z_n^{(2)}(z)\right]\overline{Y}_u^{(1)}(y)Z_v^{(1)}(z)\mathrm{d}y\mathrm{d}z,\tag{A.4}$$

$$Q_{mn}^{(3)}=-\int_{-h_2}^{0}\int_{-B}^{B}\left[\sum_{m=-M}^{M}Y_m^{(2)}(y)\sum_{n=1}^{N}\lambda_{mn}^{(2)}\mathrm{e}^{\lambda_{mn}^{(2)}(x-x_2)}Z_n^{(2)}(z)\right]\overline{Y}_u^{(1)}(y)Z_v^{(1)}(z)\mathrm{d}y\mathrm{d}z.\tag{A.5}$$

For the diffraction problem, the forced term is denoted by

$$X_{mn}^{(1)} = \int_{-h_1}^{0}\int_{-B}^{B}\left[-\mathrm{i}k_x \mathrm{e}^{-\mathrm{i}(x-x_1)k_x}\mathrm{e}^{\mathrm{i}y k_y} Z_1^{(1)}(z)\right]\overline{Y}_u^{(1)}(y) Z_v^{(1)}(z)\,\mathrm{d}y\mathrm{d}z\,. \tag{A.6}$$

However, for the radiation problem, the forced term is

$$X_{mn}^{(1)} = 0\,. \tag{A.7}$$

By substituting Eqs. (13) and (14) into Eq. (25), multiplying both sides by $\overline{Y}_u^{(2)}(y)\cdot Z_v^{(2)}(z)$ and integrating over the range $y\in[-B, B]$, $z\in[-h_2, 0]$, we obtain

$$\begin{aligned}&\int_{-h_2}^{0}\int_{-B}^{B}\left[\sum_{m=-M}^{M} Y_m^{(2)}(y)\sum_{n=1}^{N}\left(B_{mn}^{(\ell)}\lambda_{mn}^{(2)}\mathrm{e}^{\lambda_{mn}^{(2)}(x-x_1)} - \lambda_{mn}^{(2)}C_{mn}^{(\ell)}\mathrm{e}^{-\lambda_{mn}^{(2)}(x-x_2)}\right)Z_n^{(2)}(z)\right]\overline{Y}_u^{(2)}(y) Z_v^{(2)}(z)\,\mathrm{d}y\mathrm{d}z\\ &= \int_{-h_2}^{0}\int_{-w_2}^{w_2}\left[\sum_{m=1}^{M} Y_m^{(3)}(y)\sum_{n=1}^{N}\left(D_{mn}^{(\ell)}\lambda_{mn}^{(3)}\mathrm{e}^{\lambda_{mn}^{(3)}(x-x_2)} - \lambda_{mn}^{(3)}E_{mn}^{(\ell)}\mathrm{e}^{-\lambda_{mn}^{(3)}(x-x_3)}\right)Z_n^{(2)}(z)\right]\overline{Y}_u^{(2)}(y) Z_v^{(2)}(z)\,\mathrm{d}y\mathrm{d}z\end{aligned}, \tag{A.8}$$

where $\overline{Y}_u^{(2)}(y)$ represents the conjugate function of $Y_u^{(2)}(y)$. The separation process of unknown coefficient matrix in (A.6) can refer to Eq. (A.1).

Chebyshev polynomials are used to resolve the velocity singularity at the tip of the thin chamber wall. By substituting Eqs. (14) and (15) into Eqs.(26) and (27), respectively. Multiplying both sides by $Y_u^{(3)}(y)\cdot Z_v^{(2)}(z)$ and integrating over the range $y\in[-w_2, w_2]$, $z\in[-h_2, 0]$, we obtain,

$$\begin{aligned}&\int_{-h_2}^{0}\int_{-w_2}^{w_2}\left[\sum_{m=1}^{M} Y_m^{(3)}(y)\sum_{n=1}^{N}\left(D_{mn}^{(\ell)}\lambda_{mn}^{(3)}\mathrm{e}^{\lambda_{mn}^{(3)}(x-x_2)} - E_{mn}^{(S)}\lambda_{mn}^{(3)}\mathrm{e}^{-\lambda_{mn}^{(3)}(x-x_3)}\right)Z_n^{(2)}(z)\right]Y_u^{(3)}(y) Z_v^{(2)}(z)\,\mathrm{d}y\mathrm{d}z\\ &= \int_{-h_2}^{-h_3}\int_{-w_2}^{w_2}\left[\sum_{m=1}^{M} Y_m^{(3)}(y)\sum_{q=1}^{Q} Q_{mq}^{(\ell)} u_{x=x_3,q}(z)\right]Y_u^{(3)}(y) Z_v^{(2)}(z)\,\mathrm{d}y\mathrm{d}z\end{aligned}, \tag{A.9}$$

$$\begin{aligned}&\int_{-h_2}^{0}\int_{-w_2}^{w_2}\left[\sum_{m=1}^{M} Y_m^{(3)}(y)\sum_{n=1}^{N}\left(F_{mn}^{(\ell)}\lambda_{mn}^{(3)}\mathrm{e}^{\lambda_{mn}^{(3)}(x-x_3)} - G_{mn}^{(\ell)}\lambda_{mn}^{(3)}\mathrm{e}^{-\lambda_{mn}^{(3)}(x-x_4)}\right)Z_n^{(2)}(z)\right]Y_u^{(3)}(y) Z_v^{(2)}(z)\,\mathrm{d}y\mathrm{d}z\\ &= \int_{-h_2}^{-h_3}\int_{-w_2}^{w_2}\left[\sum_{m=1}^{M} Y_m^{(3)}(y)\sum_{q=1}^{Q} Q_{mq}^{(\ell)} u_{x=x_3,q}(z)\right]Y_u^{(3)}(y) Z_v^{(2)}(z)\,\mathrm{d}y\mathrm{d}z\end{aligned}. \tag{A.10}$$

By substituting Eq. (15) into Eq. (28), multiplying both sides by $Y_u^{(3)}(y)\cdot Z_v^{(2)}(z)$ and integrating over the range $y\in[-w_2, w_2]$, $z\in[-h_2, 0]$, we obtain,

$$\int_{-h_2}^{0}\int_{-w_2}^{w_2}\left[\sum_{m=1}^{M} Y_m^{(3)}(y)\sum_{n=1}^{N}\left(F_{mn}^{(\ell)}\lambda_{mn}^{(3)}\mathrm{e}^{\lambda_{mn}^{(3)}(x-x_3)} - G_{mn}^{(\ell)}\lambda_{mn}^{(3)}\mathrm{e}^{-\lambda_{mn}^{(3)}(x-x_4)}\right)Z_n^{(2)}(z)\right]Y_u^{(3)}(y) Z_v^{(2)}(z)\,\mathrm{d}y\mathrm{d}z = 0\,. \tag{A.11}$$

By substituting Eqs. (12) and (13) into Eq.(29), multiplying both sides by $\overline{Y}_u^{(2)}(y)\cdot Z_v^{(2)}(z)$ and integrating over the range $y\in[-B, B]$, $z\in[-h_2, 0]$, we obtain,

$$\int_{-h_2}^{0}\int_{-B}^{B}\left[\mathrm{e}^{-\mathrm{i}(x-x_1)k_x}\mathrm{e}^{\mathrm{i}yk_y}Z_1^{(1)}(z)+\sum_{m=-M}^{M}Y_m^{(1)}(y)\sum_{n=1}^{N}A_{mn}^{(\ell)}\mathrm{e}^{\lambda_{mn}^{(1)}(x-x_1)}Z_n^{(1)}(z)\right]\overline{Y}_u^{(2)}(y)Z_v^{(2)}(z)\,\mathrm{d}y\mathrm{d}z$$
$$=\int_{-h_2}^{0}\int_{-B}^{B}\left[\sum_{m=-M}^{M}Y_m^{(2)}(y)\sum_{n=1}^{N}\left(B_{mn}^{(\ell)}\mathrm{e}^{\lambda_{mn}^{(2)}(x-x_1)}+C_{mn}^{(\ell)}\mathrm{e}^{-\lambda_{mn}^{(2)}(x-x_2)}\right)Z_n^{(2)}(z)\right]\overline{Y}_u^{(2)}(y)Z_v^{(2)}(z)\,\mathrm{d}y\mathrm{d}z \quad (A.12)$$

By substituting Eqs. (13)and (14) into Eq. (30), multiplying both sides by $Y_u^{(3)}(y)\cdot Z_v^{(2)}(z)$ and integrating over the range $y\in[-w_2, w_2]$, $z\in[-h_2, 0]$, we obtain,

$$\int_{-h_2}^{0}\int_{-w_2}^{w_2}\left[\sum_{m=-M}^{M}Y_m^{(2)}(y)\sum_{n=1}^{N}\left(B_{mn}^{(\ell)}\mathrm{e}^{\lambda_{mn}^{(2)}(x-x_1)}+C_{mn}^{(\ell)}\mathrm{e}^{-\lambda_{mn}^{(2)}(x-x_2)}\right)Z_n^{(2)}(z)\right]Y_u^{(3)}(y)Z_v^{(2)}(z)\,\mathrm{d}y\mathrm{d}z$$
$$=\int_{-h_2}^{0}\int_{-w_2}^{w_2}\left[\sum_{m=1}^{M}Y_m^{(3)}(y)\sum_{n=1}^{N}\left(D_{mn}^{(\ell)}\mathrm{e}^{\lambda_{mn}^{(3)}(x-x_2)}+E_{mn}^{(\ell)}\mathrm{e}^{-\lambda_{mn}^{(3)}(x-x_3)}\right)Z_n^{(2)}(z)\right]Y_u^{(3)}(y)Z_v^{(2)}(z)\,\mathrm{d}y\mathrm{d}z \quad (A.13)$$

By substituting Eqs. (14) and (15) into Eq. (31), multiplying both sides by $Y_u^{(3)}(y)\cdot u_v(z)$ and integrating over the range $y\in[-w_2, w_2]$, $z\in[-h_2, -h_3]$, we obtain,

$$\int_{-h_2}^{-h_3}\int_{-w_2}^{w_2}\left[\sum_{m=1}^{M}Y_m^{(3)}(y)\sum_{n=1}^{N}\left(D_{mn}^{(\ell)}\mathrm{e}^{\lambda_{mn}^{(3)}(x-x_2)}+E_{mn}^{(\ell)}\mathrm{e}^{-\lambda_{mn}^{(3)}(x-x_3)}\right)Z_n^{(2)}(z)\right]Y_u^{(3)}(y)u_v(z)\,\mathrm{d}y\mathrm{d}z$$
$$=\int_{-h_2}^{-h_3}\int_{-w_2}^{w_2}\left[\sum_{m=1}^{M}Y_m^{(3)}(y)\sum_{n=1}^{N}\left(F_{mn}^{(\ell)}\mathrm{e}^{\lambda_{mn}^{(3)}(x-x_3)}+G_{mn}^{(\ell)}\mathrm{e}^{-\lambda_{mn}^{(3)}(x-x_4)}\right)Z_n^{(2)}(z)+\frac{\delta_{\ell,R}}{\rho gA}\right]Y_u^{(3)}(y)u_v(z)\,\mathrm{d}y\mathrm{d}z \quad (A.14)$$

The unknown coefficients $A_{mn}^{(\ell)}$, $B_{mn}^{(\ell)}$, $C_{mn}^{(\ell)}$, $D_{mn}^{(\ell)}$, $E_{mn}^{(\ell)}$, $F_{mn}^{(\ell)}$, $G_{mn}^{(\ell)}$ in Eqs. (A.1), (A.8), (A.9), (A.10), (A.11), (A.12), (A.13), and (A.14) can be solved by linear algebraic equations. In this study, to assure the numerical convergence of the present model, the infinite series are truncated at $N = 5$, $M = 20$, and $Q = 5$, respectively.

References

Arena, F., Romolo, A., Malara, G., Ascanelli, A., 2013. On Design and Building of a U-Owc Wave Energy Converter in the Mediterranean Sea: A Case Study. ASME 2013 32nd International Conference on Ocean, Offshore and Arctic Engineering.

Evans, D.V., 1978. The Oscillating Water Column Wave-Energy Device. Ima Journal of Applied Mathematics. 22(4), 423-433.

Evans, D.V., 1982. Wave-Power Absorption by Systems of Oscillating Surface Pressure Distributions. Journal of Fluid Mechanics. 114(1), 481-499.

Evans, D.V., Linton, C.M., 1993. Edge Waves Along Periodic Coastlines. The Quarterly Journal of Mechanics and Applied Mathematics. 4(46), 643-656.

Evans, D.V., Porter, R., 1995. Hydrodynamic Characteristics of an Oscillating Water Column Device. Applied Ocean Research. 17(3), 155-164.

Falcão, A.F.D.O., 2010. Wave Energy Utilization: A Review of the Technologies. Renewable and Sustainable Energy Reviews. 14(3), 899-918.

Falcão, A.F.O., Henriques, J.C.C., 2016. Oscillating-Water-Column Wave Energy Converters and Air Turbines: A Review.

Renewable Energy. 85, 1391-1424.
Falnes, J., Kurniawan, A., 2020. Ocean Waves and Oscillating Systems: Linear Interactions Including Wave-Energy Extraction. Cambridge University Press.
John Ashlin, S., Sundar, V., Sannasiraj, S.A., 2016. Effects of Bottom Profile of an Oscillating Water Column Device On its Hydrodynamic Characteristics. Renewable Energy. 96, 341-353.
Li, Y., Zhao, X., Zou, Q., Geng, J., 2022. Hydrodynamic Performance of Dual-Chamber Oscillating Water Column Array Under Oblique Waves. Physics of Fluids. 34(11), 117112.
Malmo, O., Reitan, A., 1985. Wave-Power Absorption by an Oscillating Water Column in a Channel. Journal of Fluid Mechanics. 158, 153-175.
Martins-Rivas, H., Mei, C.C., 2009. Wave Power Extraction From an Oscillating Water Column at the Tip of a Breakwater. Journal of Fluid Mechanics. 626, 395-414.
Ning, D., Ke, S., Mayon, R., Zhang, C., 2019. Numerical Investigation On Hydrodynamic Performance of an Owc Wave Energy Device in the Stepped Bottom. Frontiers in Energy Research. 7, 152.
Portillo Juan, N., Negro Valdecantos, V., Esteban, M.D., López Gutiérrez, J.S., 2022. Review of the Influence of Oceanographic and Geometric Parameters On Oscillating Water Columns. JMSE. 10(2), 226.
Qin, H., Wang, Y.X., Wang, G.Y., 2013. On Caisson Breakwater with Contracted Channel and Owc Modeling. Port & Waterway Engineering. (482), 52-56.
Rayleigh, L., 1907. Iii. Note On the Remarkable Case of Diffraction Spectra Described by Prof. Wood. Philosophical Magazine. 79(14), 60-65.
Rezanejad, K., Bhattacharjee, J., Guedes Soares, C., 2013. Stepped Sea Bottom Effects On the Efficiency of Nearshore Oscillating Water Column Device. Ocean Engineering. 70, 25-38.
Rezanejad, K., Bhattacharjee, J., Guedes Soares, C., 2015. Analytical and Numerical Study of Dual-Chamber Oscillating Water Columns On Stepped Bottom. Renewable Energy. 75, 272-282.
Rodríguez, A.A.M., Flores, A.M., Ilzarbe, J.M.B., Casarín, R.S., 2021. Interaction of Oblique Waves with an Oscillating Water Column Device. Ocean Engineering. 228, 108931.
Torre-Enciso, Y., Ortubia, I., De Aguileta, L.I.L., Marqués, J., 2009. Mutriku Wave Power Plant: From the Thinking Out to the Reality. Proceedings of the 8th European Wave and Tidal Energy Conference, Uppsala Sweden.
Vicinanza, D., Lauro, E.D., Contestabile, P., Gisonni, C., Lara, J.L., Losada, I.J., 2019. Review of Innovative Harbor Breakwaters for Wave-Energy Conversion. J. Waterway, Port, Coastal, Ocean Eng. 145(4), 3119001.
Wang, G., Dong, G., Perlin, M., Ma, X., Ma, Y., 2011. An Analytic Investigation of Oscillations within a Harbor of Constant Slope. Ocean Engineering. 38(2-3), 479-486.
Wang, G., Gao, J.L., Wang, P.T., Zheng, J.H., Dong, G.H., 2017. Review On Harbor Resonance. Haiyang Xuebao. 39(11), 1-13.
Zhao, X., Zhang, Y., Li, M., Johanning, L., 2020. Hydrodynamic Performance of a Comb-Type Breakwater-Wec System: An Analytical Study. Renewable Energy. 159, 33-49.
Zhao, X., Zhang, Y., Li, M., Johanning, L., 2021. Experimental and Analytical Investigation On Hydrodynamic Performance of the Comb-Type Breakwater-Wave Energy Converter System with a Flange. Renewable Energy. 172, 392-407.
Zhao, X., Zou, Q., Geng, J., Zhang, Y., Wang, Z., 2022. Influences of Wave Resonance On Hydrodynamic Efficiency and Loading of an Owc Array Under Oblique Waves. Applied Ocean Research. 120, 103069.
Zhao, X.L., Ning, D.Z., Zou, Q.P., Qiao, D.S., Cai, S.Q., 2019. Hybrid Floating Breakwater-Wec System: A Review. Ocean Engineering. 186, 106126.

Zheng, S., Zhang, Y., Iglesias, G., 2019. Coast/Breakwater-Integrated OWC: A Theoretical Model. Marine Structures. 66, 121-135.